

Fracture in Natural and Engineered Systems

Session Organizers: Robert HABER (UIUC), Anthony INGRAFFEA (Cornell Univ.)

Keynote Lecture

Assessment of stiffened shell structures using advanced fracture and damage mechanics methods

Karl-Heinz SCHWALBE*, Wolfgang BROCKS, Alfred CORNEC, Wernfried Schönfeld, Ingo SCHEIDER, Uwe ZERBST (GKSS Research Centre)

Residual strength characterization of integrally-stiffened structures utilizing novel manufacturing technologies

B. R. SESHADRI, S. W. SMITH*, W. M. JOHNSTON, JR. (NASA Langley Research Center)

Towards modeling of fragmentation and dynamic delamination interactions in CFRP composites

Jean-Mathieu GUIMARD*, Oliver ALLIX (ENS Cachan), Nicolas PECHNIK (AIRBUS France), Pascal THEVENET (EADS France)

A damage-based cohesive model in an adaptive spacetime discontinuous Galerkin method

Reza ABEDI, Robert B. HABER* (University of Illinois at Urbana-Champaign)

A unified potential-based cohesive model of mixed-mode fracture

Gláucio H. PAULINO*, Kyoungsoo PARK, Jeffrey ROESLER (The University of Illinois at Urbana-Champaign)

Surface and embedded cracks in offshore pipelines subjected to plastic strains

Espen BERG*, Bjørn SKALLERUD, Kjell HOLTHE (Norwegian University of Science and Technology)

Automated finite element based predictions of simultaneous crack growth and delamination growth in multi-layers in advanced metallic hybrid stiffened panels using the Alcoa ASPAN-FP tool

Henry SKLYUT*, Michael KULAK, Marcus HEINIMANN, Mark JAMES (Alcoa Technical Center), Olexander V. GONDLIAKH, Roman PASHINSKIY (KPI, Kiev, Ukraine)

Crack trajectory prediction in thin shells using finite element analysis

Jake D. HOCHHALTER*, Ashley D. SPEAR, Anthony R. INGRAFFEA (Cornell University)

Analysis of localized failure in metal beams and plates

Jaka DUJC, Boštjan BRANK* (University of Ljubljana), Adnan IBRAHIMBEGOVIC (ENS Cachan)

For multiple-author papers:

Contact author designated by *

Presenting author designated by underscore

Assessment of stiffened shell structures using advanced fracture and damage mechanics methods

Karl-Heinz SCHWALBE*, Wolfgang BROCKS, Alfred CORNEC, Wernfried SCHÖNFELD, Ingo SCHEIDER, Uwe ZERBST

GKSS Research Centre, Geesthacht
Max-Planck-Strasse, D-21502 Geesthacht, Germany

Abstract

Four studies on residual strength prediction of thin-walled geometries have been carried out for validating various assessment methods under development at GKSS.

1. Riveted curved and stiffened panel, case 1

This panel represents an aircraft fuselage which was tested elsewhere, and the test results were compared with predictions using two methods:

- (a) The method based on the δ_5 type CTOD was used to characterise the material's resistance to crack extension. This technique has recently appeared as ASTM [1] and ISO [2] standards. The R-curve for the skin material was experimentally determined and extended for large amounts of crack propagation using the cohesive model. δ_5 as a driving force parameter at the crack in the skin of the fuselage was determined by a finite element analysis.
- (b) The cohesive model was the second method employed to assess the fuselage panel. For this model, a special traction–separation law and methods for determining the cohesive parameters, cohesive stress and cohesive energy, were developed [3]. The cohesive parameters were determined by means of tests on Kahn specimens.

The maximum load experienced during the test is substantially overestimated by the R-curve technique, whereas it is underestimated by the cohesive model, **Fig. 1**. The reasons for these findings will be discussed.

2. Riveted curved and stiffened panel, case 2

In this study, a similar component was analysed within a separate project. One of the aims of the study was a comparison of the analytical SINTAP/FITNET procedure with the K_R curve concept. The latter method is frequently used in aerospace applications. The thin wall option of the SINTAP/FITNET method [4] based on the δ_5 technique was applied to the riveted panel. The elastic-plastic crack opening is given by

$$\delta_{5ep} = \delta_{5e} \cdot f(L_r)^{-2} \quad (1)$$

with

$$\delta_{5e} = K^2 / (m \cdot E' \cdot \sigma_Y) \quad (2)$$

The ligament yielding parameter, L_r , is defined as

$$L_r = F/F_Y = \sigma_{ref}/\sigma_Y \quad (3)$$

The results shown in **Fig. 2** demonstrate that the linear elastic K_R curve method overestimates the failure behaviour as compared to the SINTAP/FITNET method. In addition, since the K_R predictions are beyond the yield load, they are non-conservative.

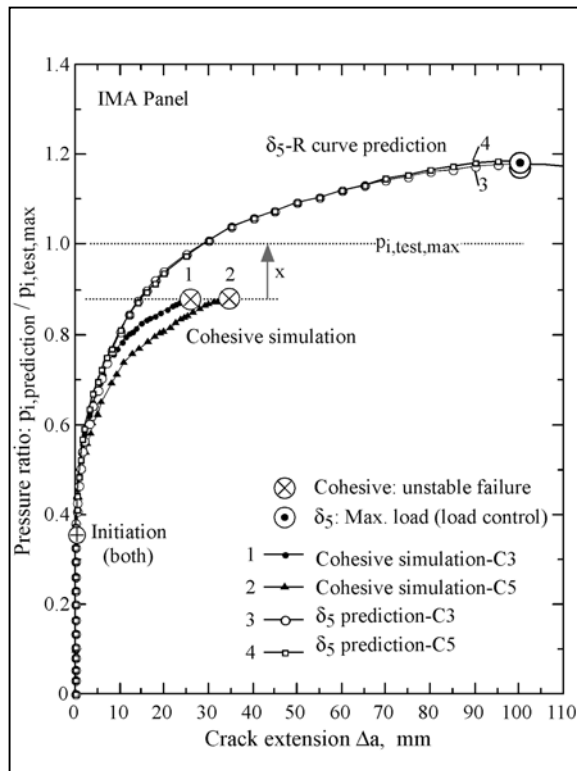


Figure 1: Assessment of a riveted curved and stiffened panel using the cohesive model and the R-curve concept.

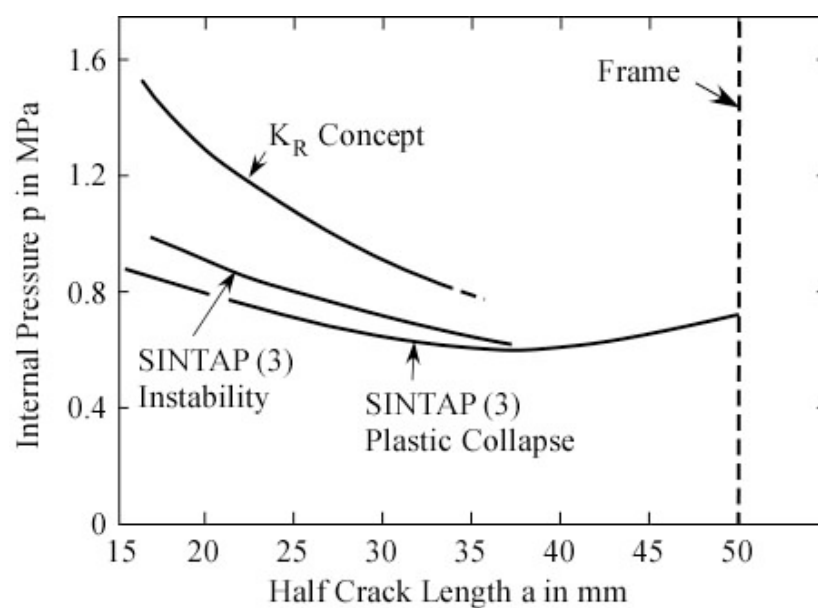
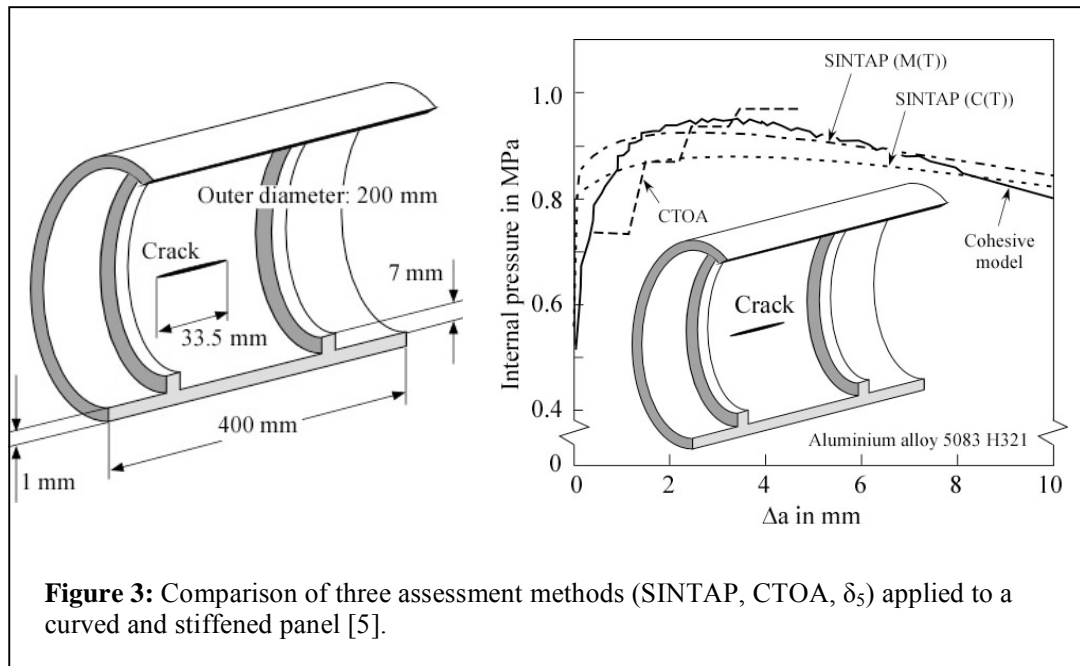


Figure 2: Predicted maximum internal pressure of a curved and stiffened panel, using the SINTAP and the K_R curve method

3. Integral curved and stiffened pressurised component

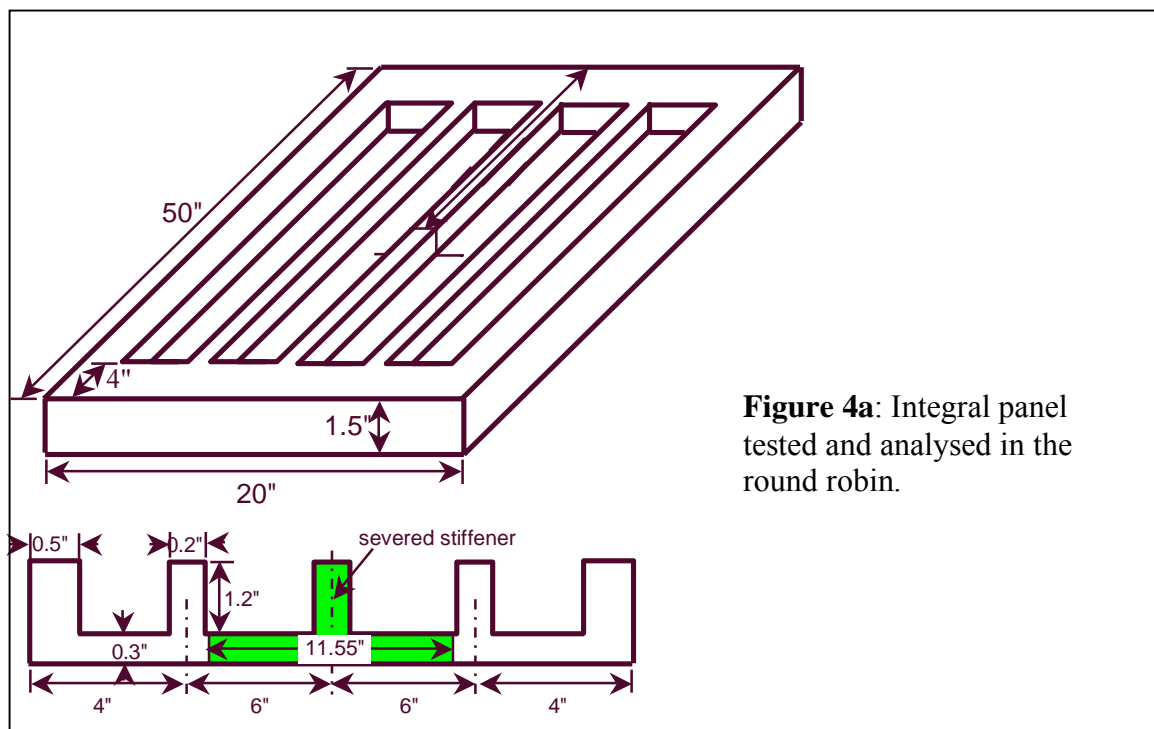
A simplified integral curved and stiffened internally pressurised component was modelled by finite elements in order to compare load versus crack extension characteristics as obtained from the methods

- Cohesive model (as in (1b) above),
- The crack tip opening angle (CTOA) method; the CTOA was measured experimentally and transferred to the panel using the FE code ANSYS,
- The thin wall module of the analytical SINTAP/FITNET procedure, see above. The results shown in **Fig. 3** demonstrate that all these methods provide very similar predictions of the maximum load.



4. Predictive round robin

Finally, this study was a contribution to a predictive round robin organised by ASTM. In this round robin, Alcoa had done a test on a tensile panel representing an integral stiffened panel with the stiffeners made by milling down a thick plate, resulting in a thin skin with stiffeners, Fig. 4a. The complexity of this study regarding the crack extension behaviour was even higher than in the previous work since the crack branched at the skin-stiffener location. Only the cohesive model could be used for such a prediction. The cohesive parameters were determined by a fit procedure to an experiment on an M(T) specimen. Again, the result was in excellent agreement with the behaviour as determined in the experiment, Fig. 4b.



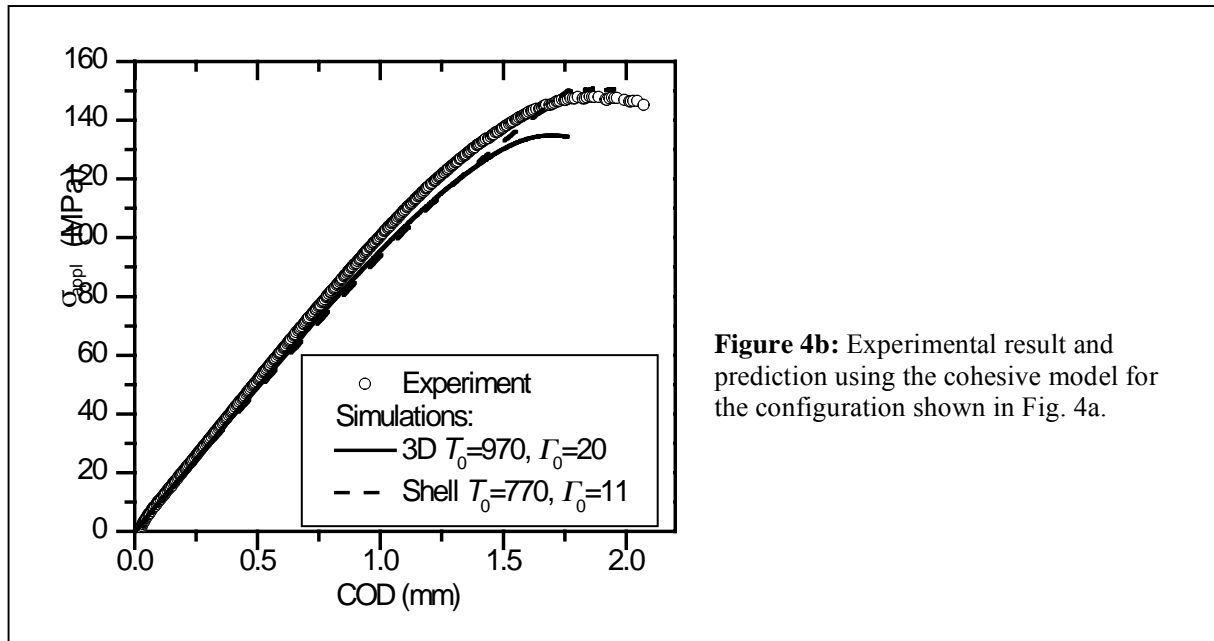


Figure 4b: Experimental result and prediction using the cohesive model for the configuration shown in Fig. 4a.

References

- [1] ASTM E 2472-06, American Society of Testing and Materials, West Conshohocken, PA, USA, 2007.
- [2] ISO 22889:2007(E), Metallic materials – Method of test for the determination of resistance to stable crack extension using specimens of low constraint, International Standards Organisation, Geneva, Switzerland, 2007.
- [3] A. Cornec, I. Scheider, K.-H. Schwalbe, On the practical application of the cohesive model. Eng Fract Mech 2003; 70: 1963-1987.
- [4] U. Zerbst, M. Schödel, S. Webster, R. Ainsworth, Fitness-for-Service Fracture Assessment of Structures Containing Cracks, Elsevier, Oxford, U.K., 2007.
- [5] U. Zerbst, A. Pempe, I Scheider, R.A. Ainsworth, W. Schönfeld, Proposed extension of the SINTAP thin wall option based on a simple method for reference load determination, submitted to Engineering Fracture Mechanics.

Residual strength characterization of integrally-stiffened structures utilizing novel manufacturing technologies

B. R. SESHADRI¹, S. W. SMITH², W. M. JOHNSTON, Jr.³
NASA Langley Research Center
Hampton, Virginia

Abstract

A finite-element fracture simulation methodology has been established at NASA Langley Research Center to predict the residual strength of damaged aircraft structures. Over the years, the prediction methodology based on critical crack-tip-opening-angle (CTOA), has been experimentally verified for laboratory coupons to full-scale built-up structural components with single and multiple-site damage. The same methodology has recently been employed in the residual strength characterization of flat and curved integrally-stiffened panels subjected to a combination of constant pressure and uniaxial tensile loading which is representative of loading conditions experienced by an aircraft fuselage in service. Analysis carried out using both two and three-dimensional finite element codes captured the crack growth and crack branching behavior in flat and curved integrally-stiffened panels. Advanced manufacturing technologies have demonstrated great promise to provide components of lower weight and containing fewer parts. The aircraft industry has expressed considerable interest in several manufacturing methods including, friction stir welding, integral machining, extrusion and electron beam free form fabrication, which are being studied at NASA Langley Research Center. To better understand the advantages and limitations of each manufacturing process, a series of panels were fabricated and tested with stiffeners either manufactured or joined using these methods. The analytical tools developed for flat and curved integrally-stiffened panels were applied to each of these test panels with specific modifications to account for multiple materials and residual stresses developed during manufacture.

Fracture tests were conducted on a series of 24-inch wide 2219 integrally-stiffened panels fabricated using friction stir welding, integral machining, extrusion and electron beam free form fabrication. Each integrally-stiffened panel had a 4 to 6-inch crack located in the center of the panel. The panels were subjected to uniaxial tension loading until failure. Load-crack extension and out-of-plane displacements were measured. The CTOA fracture criterion assumes that stable crack growth occurs when the crack-tip angle reaches a constant critical value. The critical CTOA value is determined by simulating fracture behavior in basic laboratory coupons. Middle-crack tension, M(T), or compact tension, C(T), specimens were tested to determine the critical CTOA, (Ψ_c) using a three-dimensional finite element code (ZIP3D). These values were then used in the ZIP3D analysis to predict the fracture behavior of the various integral panels. The analysis predicted stable tearing, buckling, and crack branching at the integral stiffener using the appropriate values of critical CTOA for representative material thicknesses and orientations. Comparisons are made between measured and predicted load-crack extension, strain gage measurements and out-of-plane displacement.

¹ Senior Research Scientist, National Institute of Aerospace, Hampton, VA.

² Senior Materials Research Engineer, Durability, Damage Tolerance & Reliability Branch.

³ Research Engineer, Lockheed Martin Engineering and Sciences Corporation, Hampton, VA.

1. Introduction

Widespread fatigue damage is of great significance to the operation of aging commercial transport fleets because the residual strength of a stiffened structure with a single long crack may be significantly reduced by the existence of adjacent smaller cracks as postulated by Swift [12]. Tests on wide structural panels with long-lead cracks and multi-site damage (MSD) have shown that the presence of an array of small adjacent cracks strongly degrades residual strength [2,5]. This type of damage can also lead to panel buckling, which considerably reduces the residual strength. As part of the NASA Airframe Structural Integrity Program [2,5], a fracture simulation methodology, based on the critical-crack-tip-opening angle (CTOA), Ψ_c , was developed to predict the strength of damaged aircraft structures. It has been shown [4-6] that critical CTOA determined from a single test and analysis performed with a C(T) or M(T) specimen accurately predicts the residual strength of wide stiffened panels. The CTOA fracture criterion assumes that stable crack growth occurs when the crack-tip angle reaches a constant critical value. The critical CTOA value appears to be independent of loading, crack length, and in-plane dimensions. However, it is a function of material thickness, material orientation and local crack-front constraint. The aircraft industry is investigating the possibility of using integrally-stiffened structures with the intention of reducing part count and manufacturing cost [1,3]. Analysis carried out using two and three dimensional finite element codes incorporating CTOA methodology at NASA Langley Research Center (LaRC) has captured both the crack growth and crack branching behavior in flat and curved integrally-stiffened panels [7-10]. Advanced manufacturing technologies have demonstrated great promise to provide components of lower weight and containing fewer parts. The aircraft industry has expressed considerable interest in several manufacturing methods including, friction stir welding, integral machining, extrusion and electron beam free form fabrication, which are being studied at NASA LaRC. There has been a consistent effort at NASA LaRC to extend the critical CTOA based methodology to the analysis of integrally-stiffened panels fabricated using advanced manufacturing technologies. The authors will discuss the results from the testing and analysis of different integrally-stiffened panels fabricated using different manufacturing procedures.

2. Experiments

As part of the NASA Aircraft Aging and Durability Project, fracture tests on 24-inch wide integrally stiffened panels fabricated using different manufacturing procedures are being performed at NASA LaRC. The integrally machined and extruded panels consist of a single material (AA2219-T81). The integrally machined panel is manufactured from a plate product to produce a sheet that is nominally 0.19-inch thick with two stiffeners symmetrically placed on the panel to be spaced 8-5/8 inch apart and 0.14 inch thick. The extruded panels are the thickest panels examined with a sheet thickness of 0.29-inch, with the stiffener configuration and thickness being the same as that for the integrally machined panels. The built up (riveted), friction stir welded, and free form fabricated panels were produced using two different materials. For each process, a 0.19 inch thick sheet of AA2219-T81 was used as the panel. The built up and friction stir welded panels were produced by joining a 0.14-inch thick stiffener to the panel, with the stiffeners being spaced consistent with that of the integrally-machined and extruded panels. The free form fabricated panels were manufactured by depositing layers of material onto the AA2219-T81 sheets using AA2024 powder and an electron beam system. The deposited material was heat treated with the electron beam to develop an aged material and finally machined to produce two stiffeners spaced consistent with the other panel configurations. Additional 24-inch wide panels of the AA2219-T81 material without stiffeners (unstiffened) were also tested, as a baseline configuration. Wire electron discharge machining (EDM) was used to place a starter notch (either 3.5 or 5.5-inch length) in the middle of each panel. Each panel was then fatigue loaded to produce a precrack that is approximately 4 or 6-inch in length. Each precracked panel was subjected to uniaxial tension loading along the length of the panel allowing the crack to propagate until failure. The crack length was measured visually throughout the testing. Eight strain gages were located on each panel (four on each side) to measure the deformation. In addition, to using the data of the 24-inch wide unstiffened panels to determine a baseline residual stress, the critical CTOA was evaluated and compared to that determined using a 6-inch wide C(T) specimen. Additional 6-inch wide C(T) specimens were manufactured to determine critical CTOA for the 0.29 and 0.14-inch thick AA2219 and the 0.14-inch thick AA2024 regions of each panel.

3. Analysis results

When modeling the failure of integral structures, care must be taken to ensure the proper fracture properties (CTOA) of the material are used in strength prediction. As a crack grows with stable tearing in an integrally-stiffened panel, the crack tip passes through sections of various thicknesses and orientations, which will have their own critical CTOA. In addition, when the lead crack approaches and severs an intact integral stiffener, crack branching occurs. When crack branching occurs, the crack growth at multiple crack tips is controlled with different CTOA values.

3.1 Fracture analyses of 24-inch wide integrally-stiffened panels

The 24-inch wide integrally-stiffened panels were analyzed using ZIP3D [11]. ZIP3D is an elastic-plastic material non-linear finite element software with capabilities to carry out fatigue and fracture analysis. The load-crack extension data from the test carried out on a 24-inch wide unstiffened panel was used to predict the critical CTOA required in the residual strength prediction of integral panels. Comparison of load-crack extension data for the unstiffened panel is shown in Figure 1. The open circular and square symbols correspond to the test data and ZIP3D analysis result is represented by solid line. The filled circular symbol indicates the maximum load carried by the panel before failure. The estimated critical CTOA from the analysis was 4.8 degrees. The estimated critical CTOA was used in the residual strength prediction of the integral panel. The comparison of load-crack extension results for the integral panel made from 2219-T81 is shown in Figure 2. The experimental load-crack extension data is represented by open symbols and corresponds to both left and right crack tips respectively. The filled symbol indicates maximum load carried by the integral panel at failure. The solid line indicates ZIP3D analysis result. The insert shows the location of the intact integral stiffener. ZIP3D analysis results compare well with the experimental maximum and are within 2.5% of the test maximum load. The results have demonstrated that ZIP3D has all the capability and features that are required in the analysis of integrally stiffened panels.

References

- [1] Bucci, R. J., Kulak, M., Sklyut, H., Bray, G.H., and Warren, C. J., A Study of the Material Effect in a Simulated Integrally Stiffened Wing Plank Two-Bay Crack Scenario, In Second Joint NASA/FAA/DoD Conference on Aging Aircraft, C. E. Harris, (Ed), Williamsburg, VA., 1998.
- [2] Harris, C. E., Newman, J. C., Jr., Piascik, R. and Starnes, J. H., Jr., Analytical Methodology for Predicting the Onset of Widespread Fatigue Damage in Fuselage Structure, In *Journal of Aircraft*, 1998; **35**: 307-317.
- [3] Munroe, K., Wilkins and Gruber, M., Integral Airframe Structures (IAS) – Validated Feasibility Study of Integrally Stiffened Metallic Fuselage Panels for Reducing Manufacturing Costs, 2000, NASA/CR-2000-209337.
- [4] Newman, J. C., Jr., Seshadri, B. R., and Dawicke, D. S., Residual Strength Analyses of Stiffened and Unstiffened Panels – Part I: Laboratory Specimens, In *Engineering Fracture Mechanics*, 2003; **70**: 493-508.
- [5] Seshadri, B. R., Newman, J. C., Jr., Dawicke, D. S. and Young, R. D., Fracture Analysis of FAA/NASA Wide Stiffened Panels, In second Joint NASA/FAA/DoD Conference on Aging Aircraft, C. E. Harris, (Ed). Williamsburg, VA., 1998; 513-524.
- [6] Seshadri, B. R., Newman, J. C., Jr., and Dawicke, D. S., Residual Strength Analyses of Stiffened and Unstiffened Panels – Part II: Wide Panels, In *Engineering Fracture Mechanics*, 2003; **70**: 509-524.
- [7] Seshadri, B. R., James, M. A., Johnston, W. M., Jr., and Newman, J. C., Jr. Finite Element Fracture Simulation of Integrally-Stiffened Panels, In Fifth Joint NASA/FAA/DoD Conference on Aging Aircraft, 2001, Orlando, FL.
- [8] Seshadri, B. R., James, M. A., Johnston, W. M. Jr., Young, R. D., and Newman, J. C., Jr., Recent Developments in the Analysis of Monolithic Structures at NASA Langley, In Sixth Joint FAA/DoD/NASA Conference on Aging Aircraft, 2002, San Francisco, CA.

- [9] Seshadri, B. R., Forth, S.C., Johnston, W. M. Jr., and Domack, M. S., Residual Strength Characterization of Curved integrally Stiffened Panel, 7th Joint DOD/FAA/NASA Conference on Aging Aircraft, 2003, New Orleans, LA.
- [10] Seshadri, B. R., Forth, S.C., Johnston, W. M. Jr., and Domack, M. S., Application of CTOA/CTOD in the residual strength analysis of built-up and integral structures, 11th International Conference on Fracture, 2005, Turin, Italy.
- [11] Shivakumar, K. N. and Newman, J. C., Jr., ZIP3D - An Elastic and Elastic-Plastic Finite-Element Analysis Program for Cracked Bodies, 1990, NASA TM 102753.
- [12] Swift, T., Damage Tolerance in Pressurized Fuselages, In New Materials and Fatigue Resistant Aircraft Design, D. L. Simpson, ed., EMAS Ltd., 1987; 1-77.

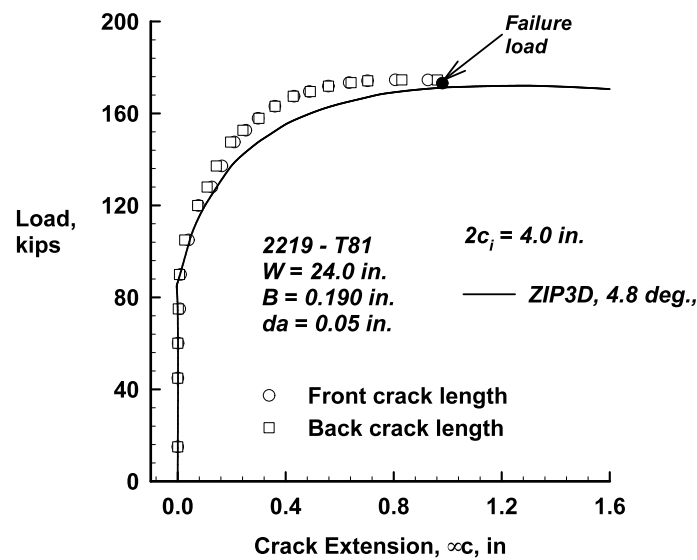


Figure 1: Load crack extension data for 24-inch wide unstiffened M(T) panel

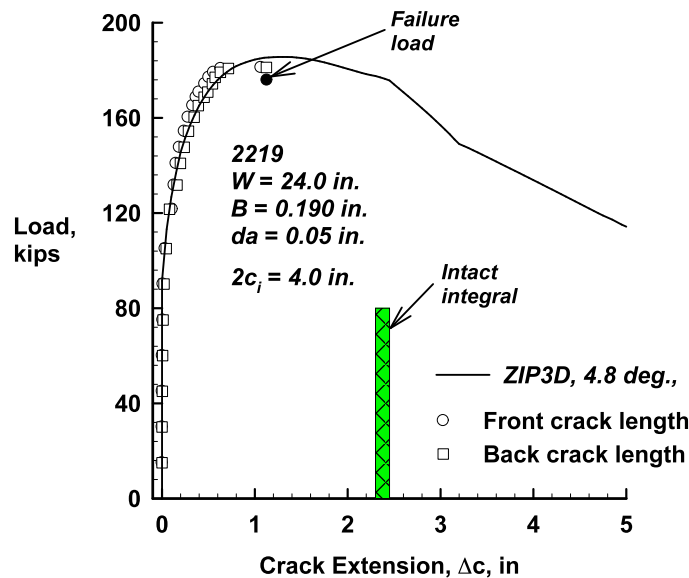


Figure 2: Load crack extension data for 24-inch wide integrally machined panel

Towards modelling of fragmentation and dynamic delamination interactions in CFRP composites

Jean-Mathieu GUIMARD^{*□}, Olivier ALLIX^{*}, Nicolas PECHNIK[°] and Pascal THEVENET[□]

^{*} LMT Cachan (ENS Cachan/CNRS/Université Paris 6/UniverSud Paris)

61, Avenue du Président Wilson, 94235 Cachan Cedex, France.

guimard@lmt.ens-cachan.fr, allix@lmt.ens-cachan.fr

[°] AIRBUS France, 316, route de Bayonne, 31060 Toulouse Cedex 03, France.

[□] EADS France, Innovation Works, 12, Rue Pasteur, 92250 Suresnes Cedex, France.

Abstract

This work deals with the numerical simulation of the dissipative phenomena involved in composite absorption devices for two main degradation modes: the ply fragmentation and the delamination process. The first one is mainly initiated by a microbuckling mechanism, which is dependant on the microstructural imperfections. The dissipated energies associated to the fragment creation are evaluated through a micromodelling approach. Contrary to expectations, these energies seem to be insensitive to microscopic parameters. On the other hand, computation control on the dynamic delamination process has been investigated through a damageable interface model. Due to quantitative crack speed records from mode II propagation tests in dynamics, we show the efficiency of a rate dependent model on the interface. We add only two new parameters to take into account these intrinsic effects, directly linked to the dynamic fracture theory. All these results give perspectives to implement delamination and fragmentation interactions at mesoscale within an absorber-like configuration.

1. Introduction

The intensive use of composite materials in the field of aeronautical structures and particularly for dynamic loading situations imposes to model by predictive methods the whole behavior up to failure. Among all the degradations involved in absorption purposes, it is now clear that the interlaminar degradation (i.e. macroscopic delamination) and the ply fragmentation are two major modes. For ply fragmentation, the key mechanism is very well known at the microscale (creation of kink-bands by a microbuckling process in longitudinal compression) but is not directly transposable for structural calculations because micro-defects a-priori trigger the mechanism. For the delamination process, numerous researches on interface modelling at mesoscale or microscale (Yu et al. [14], Corigliano et al. [4]) provide a better prediction of dynamic crack growth events in materials (Ravi-chandar [13], Lambros et al. [10]), but the physics of initiation and propagation in dynamics, and the way to include such rate dependence and at what scale are usually open issues that we proposed to discuss here.

A first part of this work is dedicated to the building of a meso-model for the fragment creation. Physical justification is based on micromechanical analyses (Fleck and al. [5]), taking into account the natural dispersive misalignments (Paluch et al. [12]) and matrix plasticity. This study enables to build a mesoscale fragmentation model improved by a statistical and only physical knowledge at microscale (Guimard et al. [7]), which gives virtual test data's for mesoscale framework. Then for the delamination issues, the objective is to enhance current interface meso-models (for example the interface developed and identified for static applications in Ladevèze et al. [9] and Allix et al. [1-2]), for the dynamic delamination process where some rate effects could occur. A recall of the different parameters influence is proposed in a derived 1D approach in dynamics and its local and global consequences when using a proposed rate dependent model. Thanks to this computational control for this new model, the identification can also be performed on mode II tests allowing good accuracy at both local (crack speeds magnitudes) and global (force versus displacement) levels.

2. Ply fragmentation modelling

2.1 1D microbuckling analysis

Over the past thirty years, many models have been proposed. In this work we have chosen a well-recognized model to treat the microbuckling process in 1D frame: the Fleck and al. model [5]. It permits an accurate description of peak instability, the process leading to a fragment creation. Although this model has not been used over the past for energy balance but for instability purposes (peak load or critical strain evaluation), the work of Guimard et al. [7] proposes calculation of peak loads and associated dissipated energies with regard to the physics of defects (figure 1).

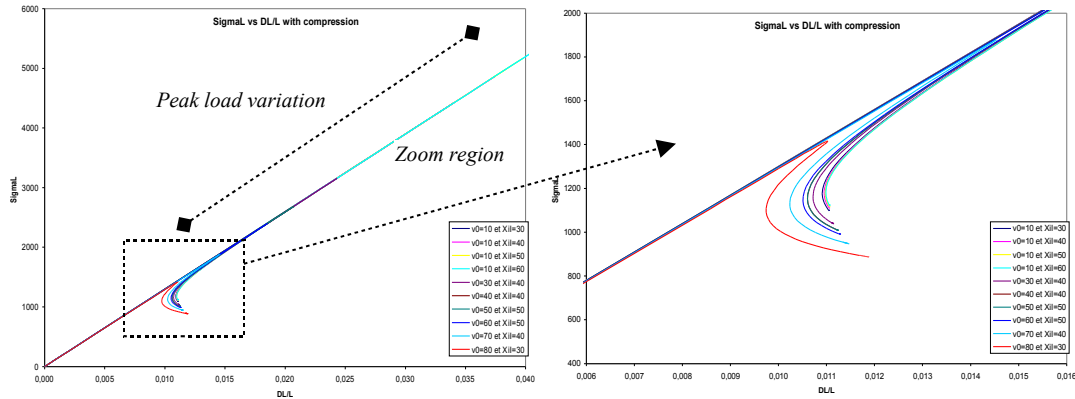


Figure 1. SigmaL vs Global Deformation (with compression part) for real imperfection couples $(\bar{q}_0; \xi_1)$.

2.2 Statistical and energetic knowledge for meso-fragmentation

These statistical results represent a virtual test database for compression failure understanding in the sense that it reproduces the key parameters influence on global behaviour in compression failure. Indeed it permits the building and improvement of a mesoscopic compression model able to treat failure, considering these microscopic knowledge with only relevant statistical data's. With this approach, we must not use all the microparameters in order to keep the conservative mechanism's evolution. Therefore, a mesoscale equivalent model can be derived with a dispersive stress parameter corresponding to the initiation and a negative hardening law which dissipate a constant energy (figure 2).

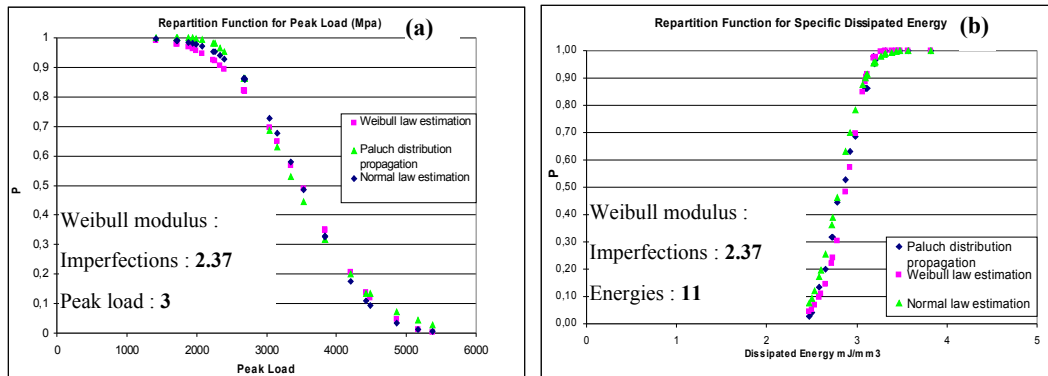
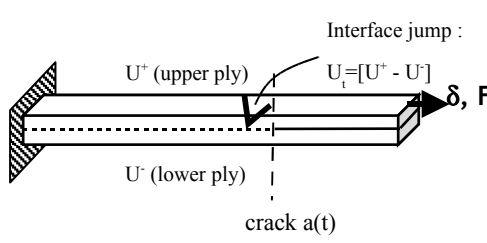


Figure 2. Identification of Peak loads repartition law (Weibull, normal) (a) and Identification of Dissipated energies repartition law (Weibull, normal) (b) for T300/914.

3. Dynamic delamination modeling by a damage interface approach

The modelling of interlaminar interface, which is chosen here, is a well known model developed at LMT Cachan and is based on damage mechanics [1-2-9]. The interface is modelled as a virtual entity with its own behavior model. We present the study of a pure mode II case: a strain energy by unit surface is first defined as follows in equations (1), the corresponding thermodynamical force associated with the internal variable d_i is then defined to give the Clausius-Duhem inequality ϕ . The classical evolution law is a rate-independent one.



$$\begin{cases}
 e_d = \frac{1}{2}(1 - d_t)k_t \left\| \bar{U}_t \right\|^2 \\
 Y_t = -\frac{\partial e_d}{\partial d_t} = \frac{1}{2}k_t \left\| \bar{U}_t \right\|^2 \text{ with } \phi = Y_t d \geq 0 \\
 d_t = f(Y) = \left(\frac{n}{n+1} \frac{\sup[\gamma Y_t(t)]}{Y_c} \right)^n \text{ if } d_t < 1 \text{ otherwise } d_t = 1
 \end{cases} \quad (1)$$

In this model, we have initiation parameters (the k_t parameter is the interface stiffness in tangent mode, n is the brittleness parameter) and propagation parameters (Y_c is the critical thermodynamical force equal to G_{Ic} , γ permits to have the G_{Ic}/G_{IIc} ratio). As a softening model, it is well known that it includes a new characteristic length which can be viewed as the process zone and influences the structural response (while any LEFM approach does not) and the mesh size required. In transient dynamics, it is also the case, but L_c is also dependent on the crack speed and we find the same magnitudes with other interface or cohesive approaches (Yu and al. [14]), the major difference is that the initiation phase is directly dependent on the stiffness and n which are physical parameters, while in classical cohesive models triangular or penalty stiffness are preferred: the consequences for physical assessment of initiation problem is crucial. For the propagation problem, the local calculation of the critical energy release rate gives a constant value and will allow crack speeds magnitudes up to the theoretical Rayleigh wave speed.

In the particular dynamic situation of mode II CLS modified, some quantitative tests (Guimard et al. [8]) have permit to conclude that a rate effect is acting on the interface (gaps in crack speeds, existence of a different limiting speed and new crack events). Among all possibilities to include a rate dependence in interface (like in Corigliano et al. [4], with a bounded jump rate), we have chosen to impose a bounded damage rate (Allix et al. [3]), which was initially used to regularize localisation problems in plies. In our dynamic situations, the key point is that this formulation (2) directly introduces a new characteristic time τ_c with a physical interpretation in terms of time to fracture, like in Morozov et al. [11], which are known to be attributed to new crack events at the microscale when the crack speed increases (Ravi-chandar [13]). We have identified the two new parameters by scanning (A_c, τ_c) couples for accurate crack speeds magnitudes (figure 3). It results in accurate correlation on the global curve (force vs. displacement) and also on the local curve (crack growth events).

$$\dot{d}_t = \frac{1}{\tau_c} [1 - \exp[-A_c \langle f(Y) - d_t \rangle_+]] \text{ if } d_t < 1 \text{ otherwise } d_t = 1 \quad (2)$$

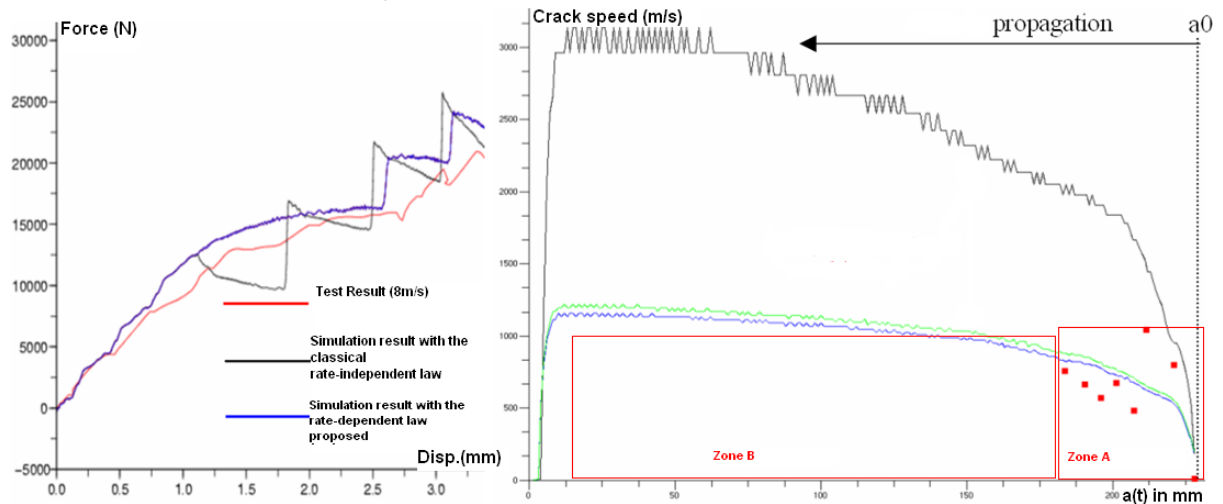


Figure 3. Comparisons between simulation and dynamic tests on a mode II CLS modified configuration: global response (left) and local response (right). The speed loading rate is 8 m/s.

The key issue is then to know if the delay effect could be linked with the dynamic fracture theory (Freund [6]). When we calculate the local critical energy release rate in the simulation, we obtain the same tendency of G_c dependence with the crack speed. So the use of a bounded damage rate allow us to take into account in an

homogenized part the physics of dynamic fracture events (Figure 4): the presence of new surfaces different from the longitudinal path, the existence of a crack limited speed and the increasing of the corresponding G_c .

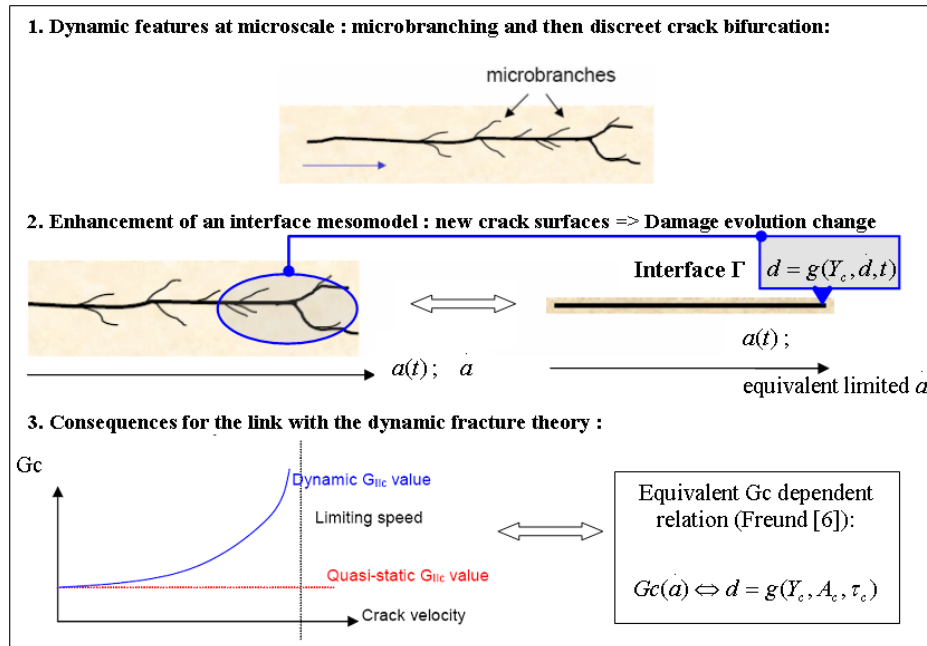


Figure 4. Overview of physics and model in high dynamic situations and consequences in terms of interface modelling enhancement for the dynamic fracture link.

Acknowledgement

This research work has been supported by Airbus France and EADS Innovation Works.

References

- [1] Allix O., L  v  que, D. and Perret, L. Identification and forecast of delamination in composite laminates by an interlaminar interface model, *Composites Science and Technology*. 58, 1998, pp. 671-678.
- [2] Allix O., Ladev  ze P., Interlaminar interface modeling for the prediction of laminates delamination, *Composite Structures* 22, 1992, pp. 235-242.
- [3] Allix, O. and De  , J.F. Damage mesomodelling for the fracture prediction of laminated composites under dynamic loading. In *Engineering Transactions*. 29-46 eds. 45(1):pp1148-1155.1997.
- [4] Corigliano, A., Mariani, S. and Pandolfi, A. Numerical analysis of rate-dependent debonding processes in composites. *Composite Structures*. 61:39-50.2003.
- [5] Fleck, N., Deng, L., Budiansky, B. Prediction of kink width in compressed fibre composites. *J. of Applied Mechanics*, 62, 1995.
- [6] Freund, L.B. Dynamic fracture mechanics. *Cambridge University Press*, 1990.
- [7] Guimard, J.M., Allix, O., Pechnik, N., Th  venet, P. Statistical energy and failure analysis of CFRP compression behavior using a uniaxial microbuckling model. *Jal of Composite Materials*. 41(23):2807-2828. 2006
- [8] Guimard, J.M., Allix, O., Pechnik, N., Th  venet, P. Characterization and modeling of intrinsic rate effects for the dynamic delamination propagation in fiber reinforced composites. *To be published in Eng. Fracture Mech. in 2008*.
- [9] Ladev  ze P. Le Dantec E., Damage modeling of the elementary ply for laminated composites, *Composite Science and Technology*, 43-3, 1992, pp. 257-267.
- [10] Lambros, J. and Rosakis, A. Dynamic crack initiation and growth in thick unidirectional graphite/epoxy plates. *Composites Science and Technology*. 57:55-65.1997.
- [11] Morozov, N.F. and Petrov, Y.V. Incubation time based testing of materials. *European J. of Mechanics A/Solids*. 25:pp 670-676. 2006.
- [12] Paluch, B. Analysis of geometric imperfections in fibres for unidirectional fibre reinforced composites. *La Recherche A  ronautique*, 6, 1994.
- [13] Ravi-chandar, K. Dynamic fracture. 2004. Elsevier Ltd.
- [14] Yu, C., Pandolfi, A., Ortiz, M., Coker, D. and Rosakis, A. 3D-modeling of intersonic shear-crack growth in asymmetrically loaded UD composite plates. *Int. J. of Solids and Structures*, 39:2779-2811, 2002.

A damage-based cohesive model in an adaptive spacetime discontinuous Galerkin method

Reza ABEDI and Robert B. HABER*

*Department of Mechanical Science & Engineering
University of Illinois at Urbana-Champaign
1206 West Green Street, Urbana, IL 61801 USA
r-haber@uiuc.edu

Abstract

We describe a new method for modeling elastodynamic fracture using a spacetime discontinuous Galerkin (SDG) finite element method and a novel, damage-based cohesive model. The underlying SDG formulation features powerful h -adaptive meshing capabilities, exact balance of linear and angular momentum on every spacetime element, good shock-capturing properties and scalable performance with linear complexity in the number of elements. Enhanced adaptive meshing capabilities provide a flexible framework for extending cohesive interfaces to track solution-dependent crack paths. Rather than use a traditional traction-separation law, we propose a damage-based cohesive model that properly accounts for the change in the structure of the interface conditions between the undamaged and fully fractured states. In so doing, the model incorporates favorable aspects from both intrinsic and extrinsic fracture models.

1. Introduction

This work describes a new method for modeling elastodynamic brittle fracture using a spacetime discontinuous Galerkin (SDG) finite element method and a novel, damage-based cohesive model. In previous work [1,2,3], we proposed an h -adaptive SDG model for elastodynamic fracture that delivers exact balance of linear and angular momentum on every spacetime element, superior shock-capturing properties and scalable, linear complexity in the number of elements. Independent error indicators, for energy dissipation and cohesive work of separation, drive the adaptive meshing process. The resulting high-precision solutions led to the discovery of quasi-singular velocity response in elastodynamic fracture and the first transient studies of the nonlinear relation between crack-tip velocity and process-zone size. Our previous implementation was restricted to problems where the potential crack paths can be determined *a priori*. Here, we introduce an improved method that supports predictions of crack propagation along trajectories determined during the solution process. The new advancing-front solution method, in which patch-wise finite element solutions are interleaved with unstructured spacetime mesh generation, supports unrestricted evolution of crack geometry while maintaining the quality of the spacetime mesh.

Most cohesive models use traction-separation laws to model the transition of material from the undamaged state to the fully separated condition. *Intrinsic* cohesive models use a large initial cohesive stiffness to approximate the compatibility constraint for undamaged material; this approximation can be problematic, especially in simulations of dynamic brittle fracture. *Extrinsic*, initially-rigid cohesive models have so far proved more suitable for brittle fracture, but these models do not describe the gradual loss of stiffness prior to reaching the cohesive strength and are generally not differentiable. The latter property is not a practical concern in explicit time integration schemes, but it does present a serious problem in the implicit patch-wise solutions used in the SDG approach. We propose a new class of cohesive models that uses a damage parameter to smoothly transition from the continuum jump conditions that describe compatibility and momentum balance in the undamaged state to the jump conditions that describe the traction-free condition in the fully separated state. This model is differentiable, describes compatibility in the undamaged state to within the accuracy of the discretization, and includes the gradual loss of stiffness prior to reaching the cohesive strength.

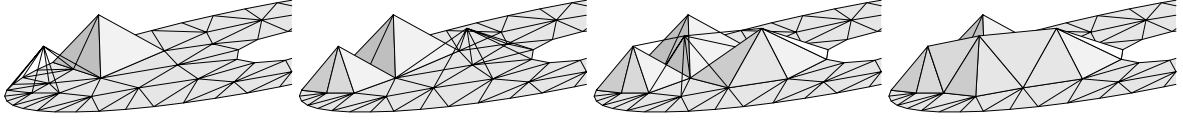


Figure 1. Pitching tents (patches) in spacetime. Local causality constraint limits patch duration; time-axis is vertical.

2. Adaptive SDG method for elastodynamics

2.1. SDG finite element formulation for elastodynamics

Our method inherits the favorable properties of the SDG method for elastodynamics [1]. It uses basis functions defined on fully unstructured spacetime meshes to describe displacement solutions that admit jumps across all inter-element boundaries. This discontinuous solution structure leads to exact balance of linear and angular momentum on every spacetime element and superior shock-capturing properties. When implemented on suitable spacetime grids, the SDG method exhibits linear complexity in the number of elements. The SDG formulation easily incorporates cohesive damage models. Displacement jumps are intrinsic to the model, so the only modification is the use of the cohesive traction model to define the target momentum flux on cohesive interfaces. There is no need for cohesive elements or other special data structures.

We use differential forms and the exterior calculus on manifolds to obtain a direct, coordinate-free notation that facilitates our formulation on unstructured spacetime meshes (*cf.* [1] for details). We have *displacement* \mathbf{u} , *spacetime momentum flux* \mathbf{M} , *body force* \mathbf{b} , *strain-velocity* $\boldsymbol{\varepsilon}$. The discrete weighted residual statement for balance of linear momentum and kinematic compatibility takes the following form: Find $\mathbf{u} \in \mathcal{V}_h$ such that, for all elements Q in the spacetime domain,

$$\begin{aligned} \int_Q \dot{\mathbf{u}} \wedge (d\mathbf{M} + \rho\mathbf{b}) + \int_{\partial Q} \left\{ \dot{\mathbf{u}} \wedge (\mathbf{M}^* - \mathbf{M}) + (\boldsymbol{\varepsilon}^* - \boldsymbol{\varepsilon}) \wedge i\hat{\mathbf{M}} \right\} \\ + \int_{\partial Q^{\text{ti}}} k\hat{\mathbf{u}}_0 \wedge (\mathbf{u}^* - \mathbf{u}) \star dt = 0 \quad \forall \hat{\mathbf{u}} \in \mathcal{V}_h^Q, \end{aligned} \quad (1)$$

in which a superposed “ \cdot ” indicates a weight function, and k is a constant introduced for dimensional consistency. \mathcal{V}_h is the discrete space of discontinuous Galerkin functions over the full space-time domain, and \mathcal{V}_h^Q is the restriction of \mathcal{V}_h to element Q . Items marked with asterisks are target fluxes that are computed from prescribed boundary or initial data, as Godunov values from the solution to a local Riemann problem on interior boundaries, or from cohesive values based on the particular fracture model at hand. The Stokes theorem applied to (1) leads to the discrete weak form that defines our finite element method:

$$\begin{aligned} \int_Q (-d\dot{\mathbf{u}} \wedge \mathbf{M} + \dot{\mathbf{u}} \wedge \rho\mathbf{b}) + \int_{\partial Q} \left\{ \dot{\mathbf{u}} \wedge \mathbf{M}^* + (\boldsymbol{\varepsilon}^* - \boldsymbol{\varepsilon}) \wedge i\hat{\mathbf{M}} \right\} \\ + \int_{\partial Q^{\text{ti}}} k\hat{\mathbf{u}}_0 \wedge (\mathbf{u}^* - \mathbf{u}) \star dt = 0 \quad \forall \hat{\mathbf{u}} \in \mathcal{V}_h^Q. \end{aligned} \quad (2)$$

It is easily shown that the discrete solution to (2) exactly satisfies the integral forms of balance of linear momentum and balance of angular momentum over every spacetime element Q [1].

2.2. Spacetime meshing

We use an advancing-front meshing/solution procedure in which the *Tent Pitcher* algorithm [4] generates unstructured spacetime meshes that obey a *causality constraint* based on the characteristics of the governing partial differential equations; see Figure 1. The causality constraint and discontinuous basis ensure that the solution on each new patch from Tent Pitcher depends exclusively on prescribed initial/boundary data and outflow data from previously-solved patches. This structure enables a scalable, patch-by-patch solution procedure with $\mathcal{O}(N)$ complexity (N is the number of spacetime elements), in which we immediately compute the local finite element solution on each new patch as soon as it is generated. The causality constraint limits the duration of each patch, but the durations of individual patches vary as there is no global time-step constraint.

We exploit this flexibility in h -adaptive analysis methods that simultaneously refine in space and time to achieve significant performance gains, especially in hyperbolic solutions with sharp wavefronts, as seen in Figure 2 (Left). The SDG scheme supports higher-order bases on fixed stencils and features an asynchronous parallel structure that facilitates high-performance implementations. In fracture applications, adaptive spacetime meshing ensures accurate resolution of sharp wavefronts and sufficient refinement in the active fracture process zone to

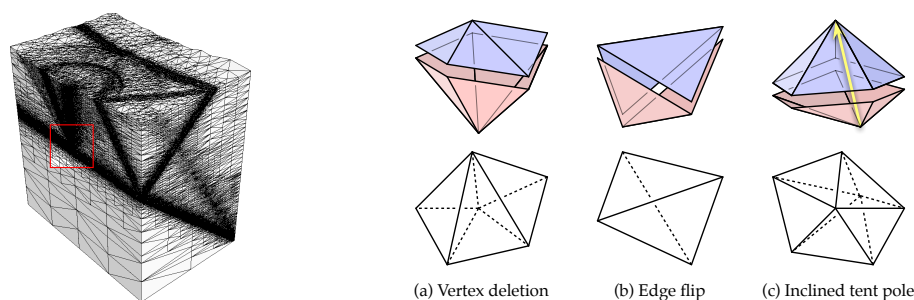


Figure 2. Left: Spacetime mesh for a crack-tip simulation with shock loads. Right: Spacetime adaptive meshing operations.

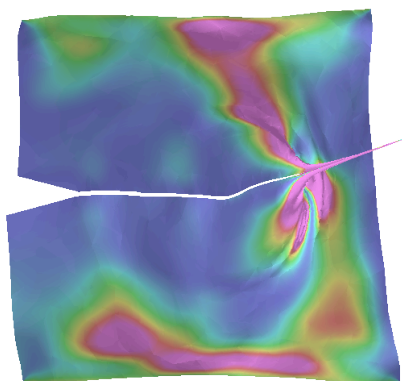


Figure 3. Dynamic fracture under mixed-mode loading showing quasi-singular velocity field

automatically ensure numerical stability and an accurate rendering of cohesive traction–separation laws. Two independent error indicators drive the adaptive procedure: a dissipation-based indicator that limits numerical energy dissipation throughout the solution domain and one that controls the discrepancy between the works of separation predicted by the trace of the finite element stress field and the cohesive traction model. The resulting high-precision solutions led to the discovery of quasi-singular velocity response in the neighborhood of the process zone and the first transient studies of the nonlinear relation between crack velocity and process-zone size.

In new work reported here, we extend the adaptive meshing capabilities to support solution-dependent nucleation and extension of cohesive surfaces. We have extended Tent Pitcher to implement common adaptive remeshing operations as special spacetime patches that incur zero projection error; Figure 2 (Right). We introduce a new set of spacetime adaptive meshing operations where each operation is implemented as a special spacetime patch rather than as a discrete operation in space. The inflow faces of the special patches conform to the outflow faces of previously solved elements, so there is no need to project the old solution onto a new mesh. This eliminates the projection errors incurred by conventional adaptive remeshing procedures and preserves the full convergence rates of high-order elements. Patches with *inclined tent poles* reposition vertices in the space mesh; we use these to continuously smooth the space mesh to maintain and improve its quality and to track moving interfaces, such as cohesive surfaces. Special single-tetrahedron patches perform *edge-flip operations* to improve the quality of the spatial triangulation. *Coarsening patches* remove a vertex from the space mesh. Mesh refinement involves a nested subdivision of the space mesh that incurs zero projection error. We use these operations in combination to nucleate cohesive interfaces at arbitrary locations and to extend existing interfaces in any direction, as indicated by the physics of the solution. Element quality is maintained throughout the procedure, and there are no restrictions on the direction of crack propagation. Figure 3 shows an example of dynamic crack propagation under mixed-mode loading conditions.

2.3. Cohesive model

Initially-rigid cohesive models are often used to simulate dynamic fracture, especially in combination with explicit time integration. These models transition abruptly from an undamaged state to the regime of a traction-separation law, and are, therefore, non-differentiable. This makes them unsuitable for our patch-wise-implicit SDG solution scheme. We propose a new initially-rigid cohesive model that uses a damage parameter to transition smoothly between enforcing the flux conditions for undamaged material and the traction-free conditions for a crack.

2.3.1. Modification of SDG formulation to incorporate a cohesive model

It is relatively easy to extend the SDG formulation for elastodynamics to incorporate a cohesive model. The SDG bases naturally support discontinuous displacements, velocity and stress across element boundaries. So the only modification required is to compute values for M^* and ε^* consistent with the cohesive model on cohesive faces. Cohesive interfaces are material interfaces, and this simplifies the formulation: M^* and ε^* simplify to σ^* and v^* , the *stress/traction form* and the *velocity form*, respectively. All that is required to implement a traditional cohesive traction separation law is (1) to set $v^* = v$ (the trace of the element velocity field on the cohesive face) to relax the velocity jump condition across the cohesive surface, and (2) set $\sigma^* = \sigma^C$, where σ^C is the cohesive traction predicted by the TSL.

In developing a new damage-based cohesive model, we attempt to combine the best properties of extrinsic and intrinsic cohesive models in a single formulation. Consider a perfectly brittle fracture process at the microstructure level, and let D be the area fraction of the cohesive surface that has fractured due to micro-crack formation. Then we have microscopic target values $\bar{\sigma}^* = \mathbf{0}$ and $\bar{v}^* = v$ on the damaged area fraction D , vs. $\bar{\sigma}^* = \sigma^G$ and $\bar{v}^* = v^G$ on the intact area fraction $1 - D$. Applying these conditions in the SDG weighted residual expression at the microstructural level and integrating to get a simple homogenization, we obtain the macroscopic target values,

$$\sigma^* = (1 - D)\sigma^G \quad (3)$$

$$v^* = (1 - D)v^G + Dv. \quad (4)$$

in which a superscript ‘G’ refers to a Godunov value obtained from the local Riemann problem for intact material. Quantities with no superscript are traces from the interiors of elements adjacent to the cohesive interface. A single dimensionless damage parameter D evolves according to a rule of the form,

$$\dot{D} = f(\sigma^\pm, v^\pm, u^\pm, D) \quad (5)$$

in which a superscript ‘ \pm ’ denotes the traces from both sides of the interface. We report on evolution models similar in structure to those proposed in [5], except we do not introduce an interface stiffness. Thus, we avoid a key disadvantage of intrinsic models that modify the bulk material properties whenever cohesive surfaces are introduced, especially as their spacing approaches zero. Provided that $D = 0$ initially, cohesive surfaces can be introduced at any density without affecting the bulk properties in the present model. In contrast to many extrinsic models, the cohesive surfaces can sustain increasing loads, so that crack nucleation and propagation can be determined intrinsically by the eventual damage evolution.

2.3.2. Propagation of cohesive surfaces

We nucleate and propagate cohesive surfaces at locations where an effective stress exceeds a critical value. Existing cohesive surfaces extend in the direction that maximizes the trace of the effective stress at the current tip of the cohesive zone, provided a specified critical value is exceeded. The flexibility of our adaptive spacetime meshing scheme allows complete freedom to follow this criterion wherever it is active and in any direction for extension.

Acknowledgment: This work was supported by the Center for Process Simulation & Design, University of Illinois at Urbana Champaign under U.S. National Science Foundation grant DMR-01-21695.

REFERENCES

- [1] R. Abedi, R. B. Haber and B. Petracovici. “A spacetime discontinuous Galerkin method for elastodynamics with element-level balance of linear momentum”. *Comp. Methods Appl. Mech. Engng.*, Vol. **195**, 3247–3273, 2006.
- [2] R. Abedi, R. B. Haber, S. Thite and J. Erickson. “An h-adaptive spacetime-discontinuous galerkin method for linear elastodynamics”. *European Journal of Computational Mechanics*, Vol. **15**, 619–642, 2006.
- [3] R. Abedi, S.-H. Chung, M. A. Hawker, J. Palaniappan, and R. B. Haber. “Modeling Evolving Discontinuities with Spacetime Discontinuous Galerkin Methods”. In *IUTAM Bookseries*, Vol. **5**; *Discretization Methods for Evolving Discontinuities*, Springer, 59–87, 2007.
- [4] R. Abedi, S. H. Chung, J. Erickson, Y. Fan, M. Garland, D. Guoy, R. B. Haber, J. Sullivan, and Y. Zhou. “Space-time meshing with adaptive refinement and coarsening”. In *Proc. 20th Annual ACM Symp. on Comp. Geometry*, 300–309, 2004.
- [5] O. Allix, P. Feissel, and P. Thévenet. “A delay damage mesomodel of laminates under dynamic loading: basic aspects and identification issues”. *Comp. & Structs.*, Vol **81**, 1177–1191, 2003.

A unified potential-based cohesive model of mixed-mode fracture

Glaucio H. PAULINO*, Kyoungsoo PARK, Jeffery ROESLER

Department of Civil and Environmental Engineering
The University of Illinois at Urbana-Champaign, Urbana, IL 61801
paulino@uiuc.edu; kpark16@uiuc.edu; jroesler@uiuc.edu

Abstract

Cohesive zone models have been widely utilized in order to investigate nonlinear fracture behavior. Several potential-based cohesive constitutive models have been proposed by, for example, Beltz and Rice (1991), Tvergaard and Hutchinson (1993), and Xu and Needleman (1993, 1994). However, previous potential-based models have limitations to represent different fracture energies in mode I and mode II. In this study, a novel potential-based cohesive constitutive model, called the PPR model, is presented in conjunction with macroscopic fracture parameters, i.e. fracture energies, cohesive strength and shape of cohesive interactions. The proposed model is able to characterize different fracture energies and cohesive strengths. The model is applicable to various material softening responses, i.e. plateau-type, brittle and quasi-brittle, due to the controllable softening shape. Furthermore, initial slope indicators are introduced to control elastic behavior, which exists in intrinsic cohesive zone models. The limits of the initial slope indicators lead to the potential model for extrinsic cohesive zone models. The consistency of the proposed constitutive model is verified by investigating path dependence of work-of-separation and simulating mixed-mode bending tests.

1. Introduction

For the analysis of deformation and failure mechanisms, one can employ either non-potential-based models (Yang and Thouless [1]; Camanho and Davila [2]; Zhang and Paulino [3]; Bosch et al. [4]) or potential-based models (Needleman [5]; Beltz and Rice [6]; Tvergaard and Hutchinson [7]; Xu and Needleman [8], [9]). Non-potential-based models are relatively simple to develop cohesive interactions because a symmetric system is not required. For instance, Yang and Thouless [1] utilized trapezoidal shaped traction-separation laws to simulate the mixed-mode fracture of plastically deforming adhesive joints. Zhang and Paulino [3] utilized the traction-based bilinear cohesive zone model for the analysis of homogeneous and functionally graded materials (FGMs) undergoing dynamic failure. Shim et al. [10] extended the traction-based model to the displacement-based bilinear cohesive zone model in order to investigate J resistant behavior of TiB/Ti FGM in conjunction with the domain integral. Bosch et al. [4] proposed an alternative exponential cohesive law, and assessed the work-of-separation under mixed-mode separation. The main limitation of a non-potential-based model is that one does not account for all possible separation or loading paths of crack growth in a domain. Therefore, some non-potential-based models may provide non-physical cohesive interactions, i.e. positive stiffness in a softening region, under certain mixed-mode fracture conditions, although the non-potential based models can capture physical fracture behavior for known crack path problems (e.g. mode I fracture or inter-layer delamination). Moreover, the tangential stiffness leads to the unsymmetric condition, which increases computational cost when solving the underlining linear system of equations.

The potential model based on a one-dimensional traction potential has been extensively employed although it is unable to represent different fracture energies in mode I and mode II [7]. However, most materials have different fracture energy with respect to the loading mode. Many researchers have demonstrated the variation of the fracture energy from mode I fracture to the mode II fracture through mixed-mode fracture specimen (Banks-Sills and Bortman [11]) and delamination testing (Reeder and Crews [12]). Due to the high fracture energy in

mode II, a structure may have higher loading capacity under certain loading conditions. A potential function which captures the different fracture energies, therefore, is necessary for the simulation of the mixed-mode fracture. A potential function which captures the different fracture energies, therefore, is necessary for the simulation of the mixed-mode fracture. In this study the authors present the previous potentials and their limitations in Section 2. A novel potential-based model is summarized in section 3.

2. Previous potentials and their limitations

Needleman [5] proposed a polynomial function-based potential to investigate void nucleation. In order to account for the limitation at the large shear displacements, Needleman [6] also developed the exponential-periodic potential based on the universal atomistic potential by Rose et al. [13]. Later, Beltz and Rice [8] obtained a generalized form of the exponential-periodic potential. The normal interaction has the exponential expression based on the atomistic potential (Rose et al. [13]), while the tangential interaction employs the periodic function due to the periodic dependence of the underlying lattice. Analogously to the exponential-periodic potential, Xu and Needleman [9], [9] proposed the exponential-exponential potential to improve the shear failure behavior.

However, the potential function proposed by Xu and Needleman, the most recent one, has several limitations because of the fracture boundary conditions and the exponential expression. First, non-symmetric boundary conditions introduce the additional length scale parameter (Δ_n^*), and result in non-physical cohesive interactions for several cases (i.e. $r \neq 0$, $q \neq 0$). When shear separation reaches infinity ($\Delta_t \rightarrow \infty$), the boundary condition for the complete normal failure, i.e. $\lim_{\Delta_t \rightarrow \infty} T_n(\Delta_n, \Delta_t) = 0$, should be introduced in the exponential potential, which

results in the symmetric boundary conditions. Instead of the boundary condition, the alternative boundary condition, $\lim_{\Delta_t \rightarrow \infty} T_t(\Delta_n^*, \Delta_t) = 0$, is utilized by introducing the additional length scale parameter (Δ_n^*). Both the

length scale parameter (Δ_n^*) and the nondimensional parameter (r) are difficult to be evaluated on the basis of either physical experiments or explanations. Because of the deficiency in the boundary condition of complete normal failure (the nonsymmetric boundary condition), when the mode I fracture energy is greater than mode II fracture energy, the cohesive interactions do not correspond to physical fracture behavior.

Next, the exponential potential originates from an atomistic potential which includes elastic behavior. When cohesive surface elements are inserted in a large domain, numerical simulations of the cohesive zone models lead to large artificial compliance. Ideally, the elastic behavior should be generally eliminated in numerical implementation of cohesive surface elements. Additionally, because of the exponential expression, the traction free condition occurs when separation is infinite, although a final crack opening width is finite in macroscopic scale fracture. The limitations of the exponential potential are summarized as follows:

- It contains an ill-defined fracture parameter, Δ_n^* , which is difficult to determine experimentally.
- It is not applicable when the mode I fracture energy is greater than the mode II fracture energy.
- It provides large artificial compliance for numerical simulation of cohesive surface elements because it does not allow any control of the elastic behavior.
- Due to the exponential function, the final crack opening width is infinite, which does not resemble macroscopic fracture behavior.

3. Unified potential-based model

As indicated above, previous potentials have several limitations such as ill-defined fracture parameters, large artificial compliance, and infinite final crack opening width. In this section, the polynomial-based potential [4] is presented in conjunction with symmetric fracture boundary conditions and macroscopic fracture parameters. The proposed potential is defined in the cohesive interaction (softening) region where fractured surfaces transfer cohesive tractions. The PPR potential satisfies the following fracture boundary conditions:

- The complete normal separation occurs ($T_n = 0$) when either normal or tangential separation reaches a certain length scale.

$$T_n(\delta_n, \Delta_t) = 0, \quad T_n(\Delta_n, \bar{\delta}_t) = 0$$

where δ_n is a normal final crack opening width, and $\bar{\delta}_t$ is a tangential conjugate final crack opening width.

- Similarly, the complete tangential separation occurs ($T_t = 0$) when either normal or tangential separation reaches a certain length scale,

$$T_n(\bar{\delta}_n, \Delta_t) = 0, \quad T_n(\Delta_n, \delta_t) = 0$$

where $\bar{\delta}_n$ is a normal conjugate final crack opening width, and δ_t is a tangential final crack opening width.

- The area under the pure normal and tangential traction-separation curves provides the mode I and mode II fracture energy, respectively,

$$\phi_n = \int_0^{\delta_n} T_n(\Delta_n, 0) d\Delta_n, \quad \phi_t = \int_0^{\delta_t} T_t(0, \Delta_t) d\Delta_t$$

- The traction-separation curves reach a peak point at a critical crack opening width (δ_{nc}, δ_{tc})

$$\partial T_n / \partial \Delta_n \big|_{\Delta_n = \delta_{nc}} = 0, \quad \partial T_t / \partial \Delta_t \big|_{\Delta_t = \delta_{tc}} = 0$$

- The traction values at the critical separations correspond to the cohesive strength,

$$T_n(\delta_{nc}, 0) = \sigma_{\max}, \quad T_t(0, \delta_{tc}) = \tau_{\max}$$

- The shape parameters (α, β) are utilized in order to represent various material softening responses. When the shape parameters are smaller than two, the cohesive law illustrates the concave shape. If $\alpha, \beta \geq 2$, the cohesive law shape is convex.

The unified mixed mode potential (PPR) and its gradients are plotted in the positive softening region, shown in Figure 1. The plotted potential represents different fracture energies (e.g., $\phi_n = 100$ N/m, $\phi_t = 200$ N/m), cohesive strengths (e.g., $\sigma_{\max} = 40$ MPa, $\tau_{\max} = 30$ MPa), cohesive laws (e.g., $\alpha = 5$, $\beta = 1.3$) and initial slope indicators (e.g., $\lambda_n = 0.1$, $\lambda_t = 0.2$). The normal cohesive law illustrates the convex shape while the tangential cohesive law describes the concave shape. Furthermore, the limits of the initial slope indicators lead to the potential model for extrinsic cohesive zone models, shown in Figure 2.

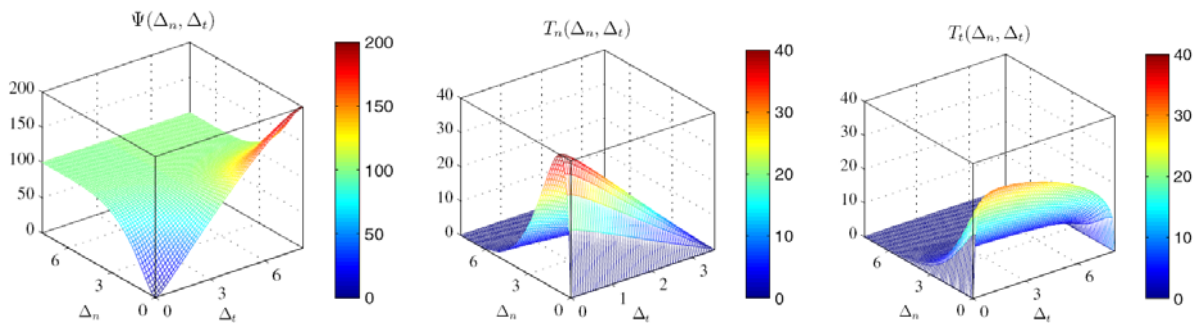


Figure 1: Unified mixed-mode potential (PPR) and its gradients for the intrinsic cohesive zone model with $\phi_n = 100$ N/m, $\phi_t = 200$ N/m, $\sigma_{\max} = 40$ MPa, $\tau_{\max} = 30$ MPa, $\alpha = 5$, $\beta = 1.3$, $\lambda_n = 0.1$, and $\lambda_t = 0.2$

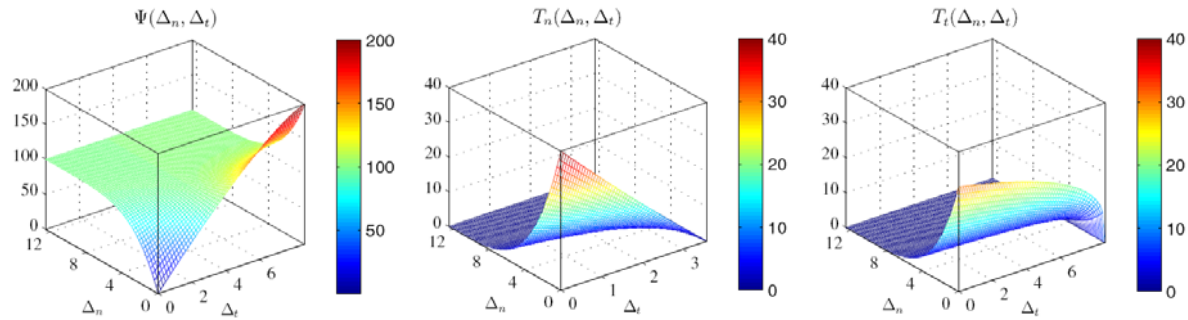


Figure 2: Unified mixed-mode potential (PPR) and its gradients for the extrinsic cohesive zone model with $\phi_n = 100$ N/m, $\phi_t = 200$ N/m, $\sigma_{\max} = 40$ MPa, $\tau_{\max} = 30$ MPa, $\alpha = 5$, and $\beta = 1.3$

3. Summary

Previous potentials have several limitations such as ill-defined fracture parameters, large artificial compliance, and infinite final crack opening width. The unified potential-based constitutive model (PPR) is presented in conjunction with physical macroscopic fracture parameters and consistent fracture boundary conditions.

References

- [1] Yang QD and Thouless MD. Mixed-mode fracture analyses of plastically-deforming adhesive joints, *International Journal of Fracture* 2001;**110**:175-187.
- [2] Camanho PP and Davila CG. Mixed-Mode Decohesion Finite Elements for the Simulation of Delamination in Composite Materials, NASA/TM-2002-211737, 2002.
- [3] Zhang Z and Paulino GH. Cohesive zone modeling of dynamic failure in homogeneous and functionally graded materials, *International Journal of Plasticity* 2005;**21**:1195-1254.
- [4] Bosch MJ, Schreurs PJG, Geers MGD, An improved description of the exponential Xu and Needleman cohesive law for mixed-mode decohesion, *Engineering Fracture Mechanics*, 2006;**73**:1220-1234.
- [5] Needleman A. A continuum model for void nucleation by inclusion debonding, *Journal of Applied Mechanics* 1987;**54**:525-531.
- [6] Beltz GE and Rice JR. Dislocation nucleation versus cleavage decohesion at crack tip, Modeling the Deformation of Crystalline Solids, Edited by Lowe, T.C., Rollett, A.D., Follansbee, P.S. and Daehn, G.S. (The Minerals, Metals & Materials Society), 1991;457-480.
- [7] Tvergaard V and Hutchinson JW. The influence of plasticity on mixed mode interface toughness, *Journal of the Mechanics and Physics of Solids*, 1993;**41**:1119-1135.
- [8] Xu XP, Needleman A. Void nucleation by inclusion debonding in a crystal matrix, *Modelling and Simulation in Materials Science and Engineering* 1993;**1**:111-132.
- [9] Xu XP and Needleman A. Numerical simulations of fast crack growth in brittle solids, *Journal of the Mechanics and Physics of Solids*, 1994;**42**:1397-1434.
- [10] Shim D-J, Paulino GH, Dodds Jr. RH. *J* resistance behavior in functionally graded materials using cohesive zone and modified boundary layer models, *International Journal of Fracture* 2006;**139**:91-117.
- [11] Banks-Sills L and Bortman Y. A mixed-mode fracture specimen: analysis and testing, *International Journal of Fracture* 1986;**30**:181-201.
- [12] Reeder JR and Crews JH. Mixed-mode bending method for delamination testing, *AIAA Journal* 1990;**28**:1270-1276.
- [13] Rose JH, Ferrante J, Smith JR. Universal binding energy curves for metals and bimetallic interfaces, *Physical Review Letters* 1981;**47**:675-678.
- [14] Park K. Paulino GH, Roesler J. A unified potential-based cohesive model of mixed-mode fracture, *submitted for journal publication*.

Surface and embedded cracks in offshore pipelines subjected to plastic strains

Espen BERG*, Bjørn SKALLERUD*, Kjell HOLTHER*

*Department of Structural Engineering
The Norwegian University of Science and Technology (NTNU)
N-7491, Trondheim, Norway
espen.berg@ntnu.no

Abstract

The present study focuses on the implementation and effects of circumferential surface and embedded cracks in pipes subjected to global bending and internal pressure. The pipe is modelled using co-rotated four-node assumed natural strain thin shell and line-spring finite elements. The embedded crack is modelled using double-defined line-spring elements which handles both centric and eccentric cracks in the thickness direction. This study is a numerical study concerning the effects of an embedded versus a surface defect.

1 Introduction

Surface cracks in curved shell structures, e.g. offshore pipelines, have been thoroughly studied the last decades. Embedded defects however has not been emphasised the same way. It is in general assumed that surface cracks are of higher criticality than embedded cracks. Fig. 1 shows the concept of a surface crack versus an embedded crack for a pipe segment. Due to the difficulties in detecting and quantifying the dimensions of an embedded crack, very little literature is available on this topic. Also it is not an easy task to fabricate an embedded crack in a large scale pipe test specimen. Nilsson et al. [10] did some fracture testing on clad flat specimens with a machined through the width embedded defect subjected to four point bending, but no experimental results for pipes are found in the literature.

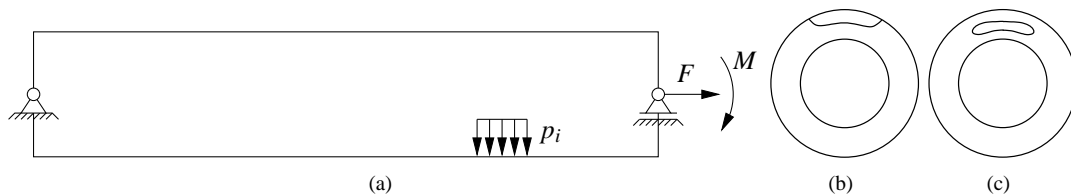


Figure 1: Schematic view of (a) a tubular pipe, and the concepts of (b) surface and (c) embedded crack

A rectangular co-rotated thin shell ANDES shell element is used for the structural modelling, and line-springs elements are used to account for a surface or embedded crack. The shell element used was first presented by Felippa and Militello [1] and further extended to account for large rotations in elastic-plastic materials by Skallerud and Haugen [5].

2 Implementation

The software employed is denoted $LINK_{pipe}$, and is based on four-node ANDES shell elements and non-linear line-spring elements. The shell element has 6 degrees of freedom in each node.

The surface crack is accounted for by line-spring elements. The line-spring elements are non-linear connectors between shell elements where the stiffness of the connector is changing with relative crack depth and material hardening. The line-spring element was initially proposed by Rice and Levy [2] and further extended by Parks and co-workers [3, 4]. The elastic-plastic line-spring element consists of tabulated convex yield surfaces, $\Phi(Q; a; t; \sigma(\epsilon^{pl}))$, where Q are the generalised forces in the line-spring element, a is the crack depth, t is the shell thickness and $\sigma(\epsilon^{pl})$ is the uniaxial stress at an equivalent plastic strain of ϵ^{pl} . As for the shell element used in the code, the line-spring element transmits stress resultants to the main program. Further details about the theory and implementation of $LINK_{pipe}$ and the line-spring element are provided by Skallerud et al. [6, 7].

The generalised forces along with the generalised displacements are used to compute the crack tip opening displacement, $CTOD$, which is used in the ductile crack growth algorithm. The ductile crack growth assumes quasi-static conditions, and the crack grows through the thickness following a crack growth resistance curve. This curve comes from either experiments or other numerical damage analyses, e.g. Gurson-Tvergaard-Needleman damage model. The implementation is also extended by Berg et al. [8] to account for circumferential crack growth in addition to the in depth crack growth. The crack growth in the thickness and circumferential directions are incrementally updated as $a^{(i+1)} = a^{(i)} + \Delta a^{(i)}$ and $c^{(i+1)} = c^{(i)} + \Delta c^{(i)}$. The implementation for surface cracked pipes is validated by Berg et al. [9] against large scale experiments of pipes subjected to internal pressure and bending load.

Embedded defect is introduced in $LINK_{pipe}$ using the surface cracked line-spring element. As shown in Fig. 2, two line-spring elements together forms the embedded defect. One element has the surface crack on the upper side and the other element has the surface crack located on the inside. Linear dependencies couples this pair of line-spring elements to the neighbouring shell elements. This method does not demand any changes of the element codes. The sum of the wall thicknesses of the two line-spring elements equals the wall thickness of the neighbouring shell elements.

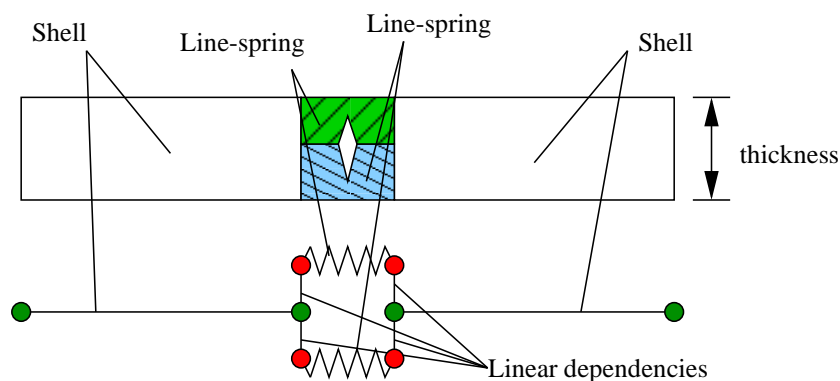


Figure 2: Conceptual figure of the modelling of embedded defects using shell and line-spring elements

3 Results

The model used in the analyses is a straight pipe segment, modelled with shell elements and line-spring elements, having an outer diameter of 400mm, a wall thickness of 20mm and a length of 6 times the outer diameter (2400mm). A transversal defect was positioned at the mid-span of the pipe length at a location of 12 o'clock. A positive bending moment will then contribute to open the crack in mode I. The surface crack is modelled with uniform initial depth of 4.0mm and a crack length of 126mm. The embedded crack has the same initial crack dimensions as the surface crack. The material properties used in the analyses are based on a linear elastic non-

linear plastic power law hardening. Young's modulus, E , is 207000MPa and Poisson's ratio, ν , is 0.3. The initial yield stress and hardening exponent are $\sigma_0 = 460\text{MPa}$ and $n = 0.07$ respectively. The pipe is subjected to a non-proportional loading situation with an internal pressure giving 40% of yield in the circumferential direction followed by a global bending moment.

Fig. 3 compares the applied global strain versus crack growth for outer and inner surface flaw and one case of embedded crack. It is observed that the internal surface crack has the highest deformation capacity and the embedded crack located between the outer surface and mid-thickness has the smallest deformation capacity. It is also observed that the ductile crack growth for embedded defect at mid-thickness is very close to the crack growth for the outer surface crack.

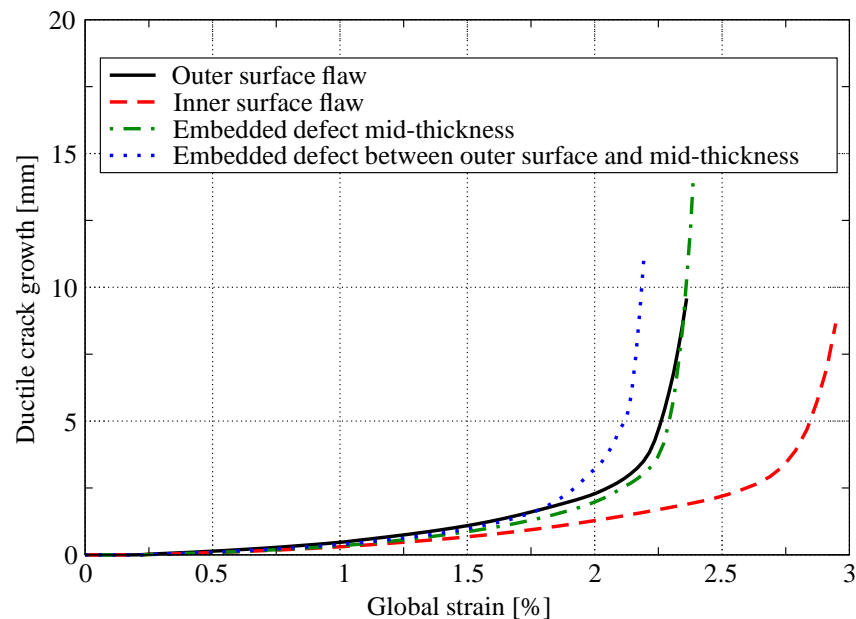


Figure 3: Global strain versus ductile crack growth for outer surface flaw, inner surface flaw, embedded defect located at the mid-thickness and embedded defect located between outer surface and mid-thickness (cf. Fig. 2)

In Fig. 4 the effect of eccentricity for the embedded defect is plotted in terms of critical strain versus crack eccentricity. The initial crack size is the same for all analyses. The crack is then moved from almost outer surface flaw to an almost inner surface flaw. The abscissa axis in Fig. 4 is the distance from the outer surface to the center of the embedded crack. It is here observed that the embedded crack closest to the outer surface has the lowest strain capacity before it breaks the surface and the crack with a distance of 12mm to the outer surface has the highest deformation capacity. It is noteworthy to see that the crack positioned with 4mm from the outer pipe surface has a lower deformation capacity than the innermost crack (4mm from the inner surface). For the case with the highest strain capacity, the crack location is such that the local bending moment contributing to open the crack is at its minimum, hence the crack opening consists of a more membrane dominated situation as for the other locations.

4 Conclusions

The present study focuses on the effect of embedded defects in a shell structure. Results for one crack depth to thickness ratio and nine locations of the crack are presented. The global load mode was internal pressure and global bending moment. The position of the crack shows that the crack close to the outer pipe surface is more critical than the crack close to the inner pipe surface. It is also observed that the embedded defects can become more critical compared to the surface cracks at higher strain levels. A crack located between the inner pipe surface and the center of the thickness has the highest strain capacity.

Due to the high plastic strains a stress based design approach is not feasible, hence a strain based design approach is recommended.

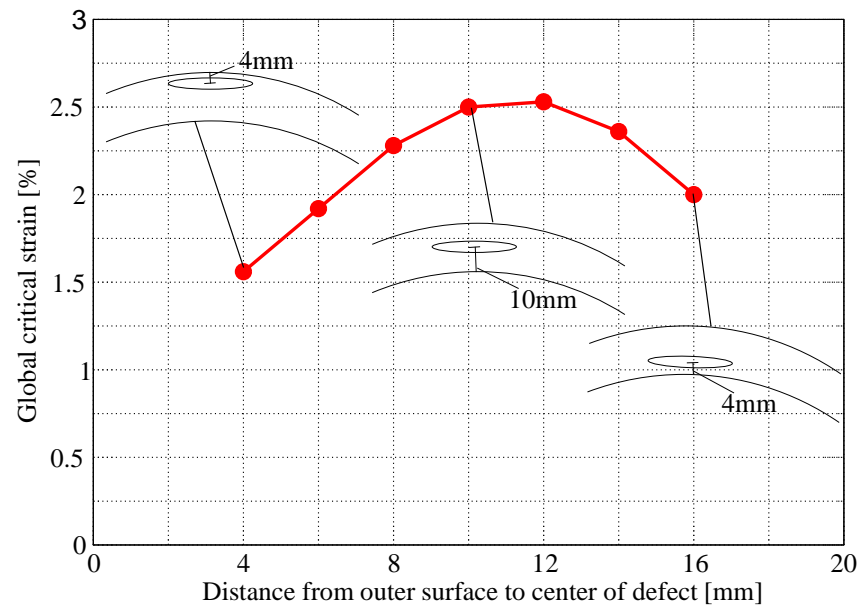


Figure 4: Distance from outer pipe surface versus the strain level when the embedded defect breaks the surface on the outer or inner pipe wall

REFERENCES

- [1] Felippa CA and Militello C. Membrane triangles with corner drilling freedoms: II. The ANDES element. *Finite Elements in Analysis and Design*, 1992;**12**:189–201.
- [2] Rice JR, Levy N. The part-through surface crack in an elastic plate. *Journal of Applied Mechanics*, 1972;**39**:185–194.
- [3] White CS, Parks DM. Elastic-plastic line-spring finite elements for surface-cracked plates and shells. *Journal of Pressure Vessel Technology*, 1982;**104**:287–292.
- [4] Lee H, Parks DM. Fully plastic analyses of plane strain single-edge-cracked specimens subjected to combined tension and bending. *International Journal of Fracture*, 1993;**63**:329–349.
- [5] Skallerud B and Haugen B. Collapse of thin shell structures – stress resultant plasticity modelling within a co-rotated ANDES finite element formulation. *International Journal of Numerical Methods in Engineering*, 1999;**46**:1961–1986.
- [6] Skallerud B, Holthe K, Haugen B. Thin shell and surface crack finite elements for simulation of combined failure modes. *Computer methods in applied mechanics and engineering*, 2005;**194**:2619–2640.
- [7] Skallerud B, Berg E, Jayadevan KR. Two-parameter fracture assessment of surface cracked cylindrical shells during collapse. *Engineering Fracture Mechanics*, 2005;**73**:264–282.
- [8] Berg E, Skallerud B, Thaulow C. Two-parameter fracture mechanics and circumferential crack growth in surface cracked pipelines using line-spring elements. *Engineering Fracture Mechanics*, 2008;**75**:17–30.
- [9] Berg E, Østby E, Thaulow C, Skallerud B. Ultimate fracture capacity of pressurised pipes with defects – Comparisons of large scale testing and numerical simulations. *Engineering Fracture Mechanics*, 2008;**75**:2352–2366.
- [10] Nilsson KF, Taylor N, Minnebo P. Analysis of fracture tests on large bend beams containing an embedded flaw. *International Journal of Pressure Vessels and Piping*, 2006;**83**:72–83.

Automated finite element based predictions of simultaneous crack growth and delamination growth in multi-layers in advanced metallic hybrid stiffened panels using the Alcoa ASPAN-FP tool

Henry SKLYUT^{1*}, Michael KULAK¹, Markus HEINIMANN¹, Mark JAMES¹, Olexander V. GONDLIAKH², Roman PASHINSKI²

*Alcoa Technical Center
100 Technical Lane
Alcoa Center, PA 15069
henry.sklyut@alcoa.com

¹ Alcoa Technical Center, Alcoa, Inc.

² National Technical University of Ukraine "KPI", Kiev, Ukraine

Abstract

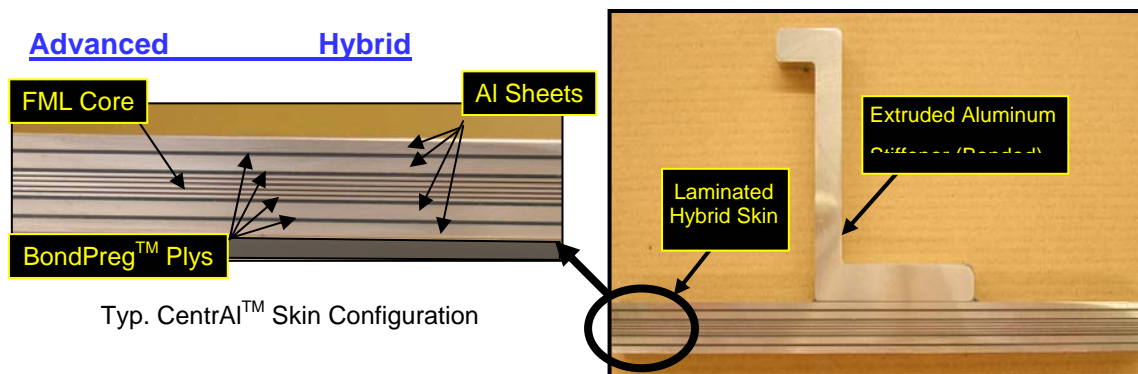
The challenging performance and affordability goals of next generation aircraft have accelerated demand for advanced structural concepts capable of achieving significant weight and cost savings. Alcoa has developed advanced metallic hybrid concepts for use in areas of fuselage and lower wing covers that are traditionally limited by static tension, fatigue and damage tolerance, and residual strength.

1. Introduction

For fuselage the concepts involve the bonding of FML reinforcing straps under stringers and/or frames only where needed to improve performance. For lower wing skins the Alcoa concepts focus on bonded laminated metallic sheet structure with embedded FML reinforcement structure (CentrAl), Figure 1, or without this FML core reinforcement structure. In all concepts the layers are bonded together using adhesive or BondPregTM which is a reinforced adhesive specially developed to optimize fatigue crack growth in advanced hybrid structures. This approach for lower wing skins allows for a degree of structural tailoring previously unseen in metallic structures, while addressing the issues of thermal expansion mismatch, galvanic corrosion and strain to failure mismatch, associated with structures assembled from graphite composites and aluminum.

Alcoa has completed several experimental programs on coupons and flat panels to validate the extraordinary performance and weight saving benefits of advanced metallic hybrid concepts, Figure 2. In addition, a large scale testing program was conducted for wing and fuselage panels to validate breakthrough improvements in structural damage tolerance performance. For wing concepts, crack growth tests were conducted on five stiffener panels with a broken central stiffener representing a repeat inspection scenario for cracks growing under wing bending loads. Again, both constant amplitude and representative wing cyclic load spectra were applied (Figure 3). For fuselage concepts, crack growth tests were conducted on five stringer panels with a broken central stringer representing a repeat inspection scenario for circumferential cracks in the crown of the fuselage (Figure 4). Both constant amplitude and representative fuselage cyclic load spectra were applied.

This presentation addresses the work aimed at developing methods to predict the fatigue crack growth in the advanced metallic hybrid stiffened panels. This work encompasses 1) the development of a methodology to grow delaminations in multiple layers within the laminated skin of the stiffened panel structure, 2) material property inputs to the delamination growth models and crack growth models, 3) the development of an self contained, user friendly finite element based software code (ASPAN-FP) which has the capability to simultaneously grow bond line delamination and metal layer cracks in multiple layers and at multiple locations in stiffened panels. This capability is needed when analyzing the effect of the bending loads introduced by a broken stiffener on crack growth and delamination growth in the skin (Figure 5) . Results of validation analyses will be presented for strap reinforced panels of various gage thicknesses run under constant amplitude loading, Figure 6-7, and for a laminated CentraITM middle crack specimen under constant amplitude loading. Finally predictions for an advanced hybrid stiffened wing panel under constant amplitude loads will be presented. Issues related to extending this approach to spectrum loading and residual strength predictions will be discussed



A stiffened structural assembly employing laminated aluminum skins reinforced by finite width FML straps and outer aluminum sheets bonded with BondPregTM fiber-reinforced adhesive

Figure 1, CentrAI Advance Hybrid Lower Wing Concept

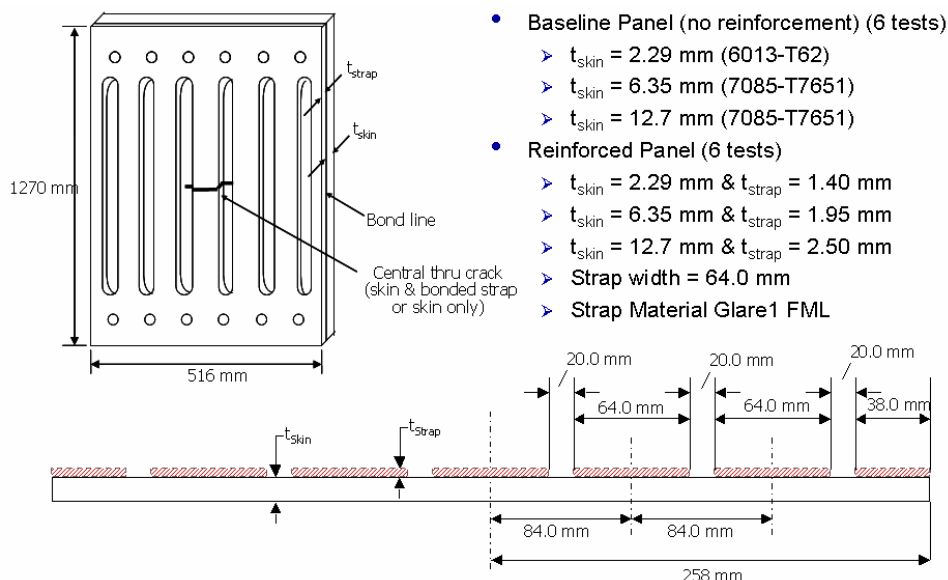


Figure 2, FML reinforced Aluminum Panels Testing Program

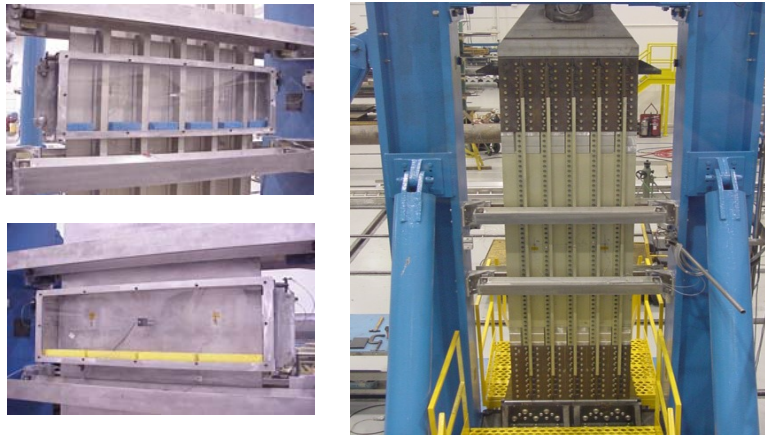


Fig. 3. Large Panels Tested under Mini-TWIST Lower Wing Spectrum and Constant Amplitude Load

■ **Testing being executed at Purdue University Bowen Large Scale Test Laboratory**

- ✓ 8.2 m (27 ft) tall test frame; 980 kN (220 kip) actuator
- ✓ Controlled environment (temp & RH in local crack plane)

■ **Test Program**

- ✓ 5 stringer crown concepts; 762 mm (30 in.) x 2,030 mm (80 in.) panels
- ✓ 2 frame concepts; 762 mm (30 in.) x 2,030 mm (80 in.) MT panels
- ✓ Testing of adv. alloy, design and mfg. concepts, including LBW
- ✓ FCG (constant amplitude, crown & frame spectra) and residual strength testing



Fuselage crown stringer panel test set-up

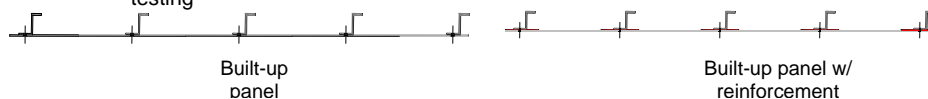


Fig. 4. Large Panels Tested under Fuselage Crown Spectrum and Constant Amplitude Load

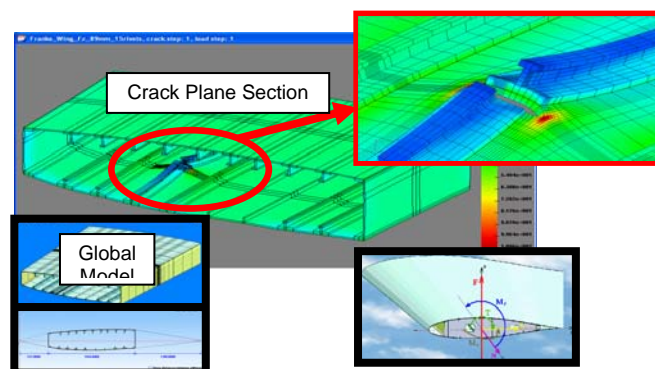


Fig. 5. Bending Loads from Broken Stiffeners introduce a non-uniform crack and delamination pattern in the laminated skin through-the-thickness.

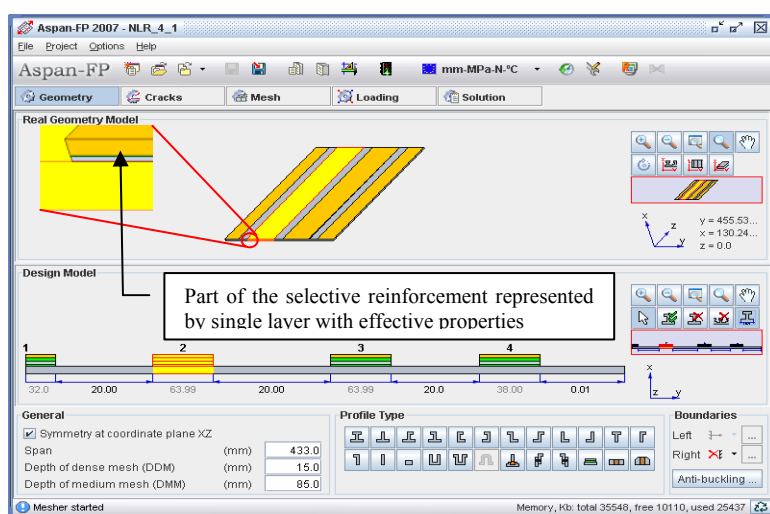


Figure 6, Aspan-FP model of the NLR panel 4.1

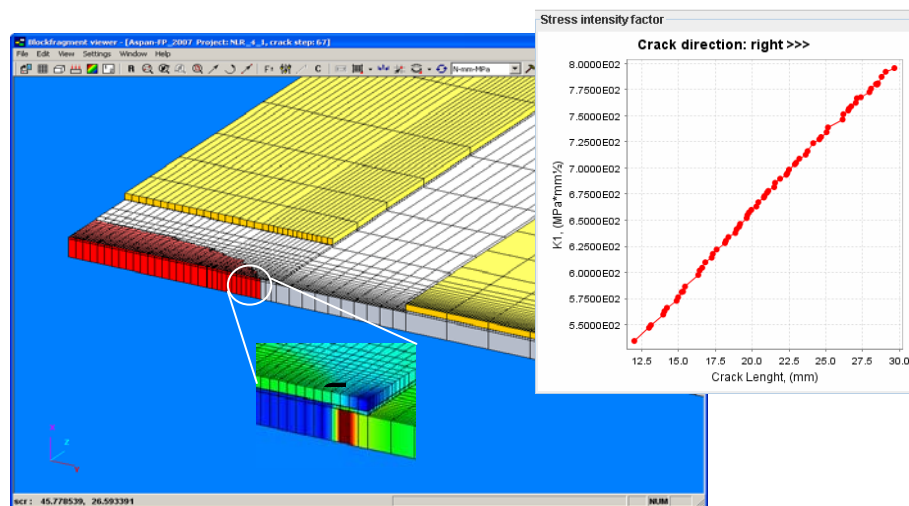


Figure 7, Skin crack and delamination modeling in Aspan-FP

References

- [1] A. S. Sacharov. Moment Schema of Finite Element Method (MSFEM) including rigid body rotation. Strength of Materials and Theory of Structures. – 1974. Vol. 24. Pages 147-15
- [2] Bucci, R.J., Kulak, M., Heinimann, M.B., Hinrichsen, J., James, M.A., Liu, J., “Advanced Hybrid Structures and Materials, ... Tailorable Solutions to Meet Demanding Use and Affordability Requirements of Future Aircraft,” Proceedings 30th ICAF Conference, National Reviews, Meeting on the International Committee on Aeronautical Fatigue, Naples, Italy, May 14-15, 2007.
- [3] Heinimann, M.B., Kulak, M., Bucci, R.J., James, M.A., Wilson, G.S., Brockenbrough, J.R., Zonker, H., Sklyut, H., “Validation of Advanced Metallic Hybrid Concept with Improved Damage Tolerance Capabilities for Next Generation Lower Wing and Fuselage Applications,” Proceedings of 24th ICAF Symposium, Durability and Damage Tolerance of Aircraft Structures: Metals vs. Composites, Napoli, Italy, May 16-18, 2007.

Crack trajectory prediction in thin shells using finite element analysis

Jake D. HOCHHALTER*, Ashley D. SPEAR, Anthony R. INGRAFFEA

*Cornell University, 640 Rhodes Hall, jdh66@cornell.edu

Abstract

The purpose of this work is to investigate crack growth trajectory within a pressurized floating-frame fuselage. Many in-depth research projects have focused on computing residual strength of aircraft structural components using thin-shell geometry models *a priori* [7, 5, 10, 4, 3]. These projects developed a modeling interface between STAGS (STructural Analysis of General Shells) and FRANC3D, a FRacture ANalysis Code. STAGS, however, is not commercially available software and is relatively limited in capability. Therefore, FRANC3D was extended to interface with ABAQUS. Much of the work presented here addresses the verification of this interface and quantifying the effects of the frames and doublers, used in a floating-frame fuselage, on crack growth trajectory. Also briefly discussed is a modeling framework that incorporates a fully 3D model near the crack front for simulation of through-thickness crack growth.

1. Introduction

To study crack trajectory, a sub-model of an aircraft fuselage of a generic narrow body fuselage was modeled using ABAQUS CAE. The fuselage panel modeled here is shown as Figure 1. The geometry shown in Figure 1 is a floating-frame design and is common to commercial transport aircraft. In addition to the components shown in Figure 1, doublers (tear straps) which run beneath the frames and are coupled to the skin were also explicitly modeled. The tear straps are detailed in Figure 2. The tear straps are important since they are designed to retard crack growth either by stopping the crack propagation or redirecting it so that it will not grow beyond a bay of the fuselage. The boundary conditions applied to this model were the result of a global/local approach where displacements and rotations were taken from the results of the global model and applied to the boundaries of the local submodel studied here. An internal pressure equal to 7.8 psi was also applied to simulate cabin pressurization during flight.

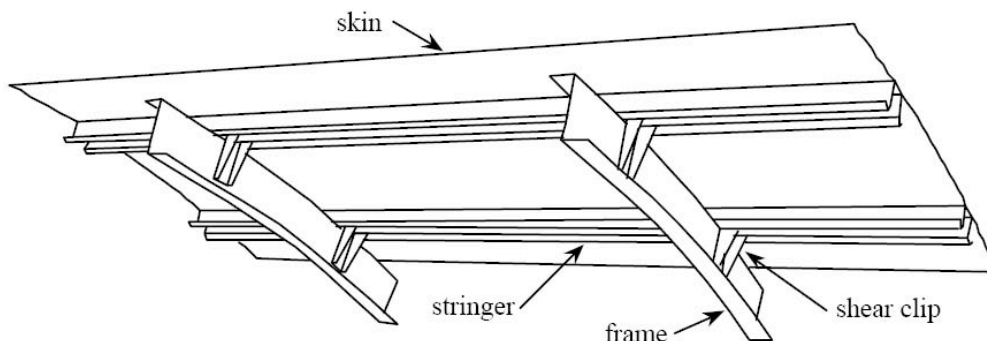


Figure 1: Aircraft fuselage section to be modeled.

2. Finite Element Model

To understand the major influences on crack trajectory, four separate models were created for this study, including:

- Case 1- Model of skin with edge boundary conditions;
- Case 2- Model of skin with edge boundary conditions and internal pressure;
- Case 3- Model of skin and tear straps with edge boundary conditions and internal pressure;
- Case 4- Complete model of Figures 1 and 2 with edge boundary conditions and internal pressure.

By successively adding detail to the geometry of the model, the contribution of the specific components to crack trajectory could be more easily understood. The trajectory results of the 4 configurations are shown in the next section.

In the analyses, the model was simulated with a 3 inch initial crack length, as shown in Figure 3. At the crack tip, quarter-point triangular elements were used. The mesh was then transitioned toward the boundaries using triangular elements and quad elements where bilinear mapping could be employed. Discrete crack growth steps were modeled in one inch increments. At each step, the crack growth direction was computed using the $\max(\sigma_{\theta\theta})$ criterion. The crack was then propagated in the computed direction, and, finally, the model geometry was updated with the new crack configuration and remeshed for subsequent analysis. Important modeling assumptions are summarized here:

1. Contributions from thin shell crack motions, k_1 and k_2 , are ignored;
2. The crack would not arrest in the skin ($K_{IC} < K_I$);
3. Material nonlinearities and fracture anisotropy were not considered;
4. T-stress effects on propagation direction were included;
5. BCs were not updated at crack growth iterations;
6. Depressurization was not considered.

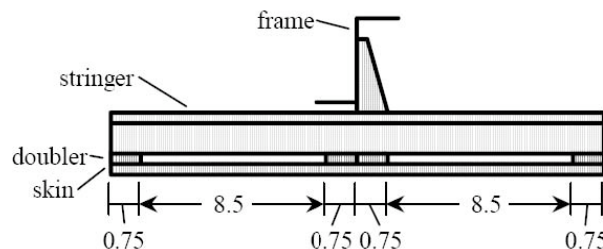


Figure 2: Typical cross-sectional view of model fuselage (dimensions shown in inches).

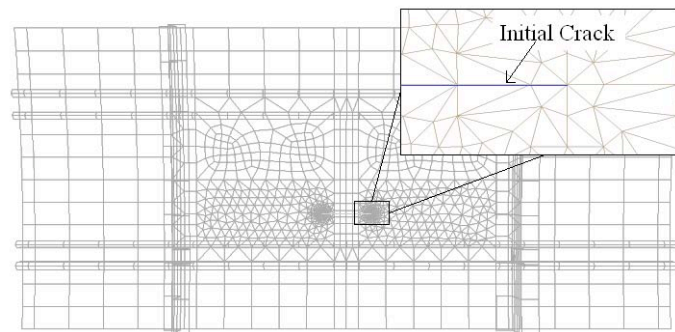


Figure 3: Meshed fuselage panels with initial crack geometry.

The FRANC3D/ABAQUS interface was implemented to complete the crack growth iterations. As shown in Figure 4, the initial model attributes are defined in ABAQUS, and FRANC3D is used to compute crack growth parameters and updates the geometry and mesh. After a model is analyzed using ABAQUS, FRANC3D computes the location of the new crack front, extends the crack, and updates the model geometry. Finally, remeshing is done and the process is continued until some criterion is met. For this study, the crack was grown in one inch increments until the crack was within 0.5 inch of the doublers.

3. Results

Figure 5 shows the predicted crack trajectories for the various levels of model detail as listed in the previous section. Case 1, the model involving only the skin with no applied pressure, is not shown in the figure since no turning of the crack occurred. This result, when compared with Case 2, shows the influence of cabin pressurization on crack trajectory. By observing the results of these simplified models, it is easy to determine

which structural components have the strongest influence on crack growth direction. In comparing Case 2 only with Case 3 it is observed that the doublers have little effect on crack growth trajectory when the tip is away from the doublers. However, as the crack approaches the doublers, their presence is felt through the change in local stress field and the crack is turned more as a result. It is also seen that the fully detailed Case 4 results in a much more dramatic turning during trajectory. This is due mainly to the introduction of the doublers. The crack was not placed symmetrically in the fuselage and was actually closer to the lower stringer. With the inclusion of the stringers, this caused more exaggerated crack turning at the beginning stages of crack growth.

To make sense of the magnitudes by which the crack turns, observe Figure 6, which is a graphical representation of the well-known, second order maximum tangential stress equation. It is seen that the two governing ratios are T/K_I and K_{II}/K_I . For both ratios, a large value results in a large θ_c . The r_c value must be defined as a unique value since the $\max(\sigma_{\theta\theta})$ direction depends on r_c and different values for r_c will produce different predicted propagation angles. For this study, it will suffice to consider r_c as a material constant that can be determined from fracture testing of coupons. The value of r_c , 0.05 inch, used here is a result of extensive coupon testing [6].

So, we see that $T = (1.5 \text{ in}^{1/2}) T/K_I$. For the initial cracked configuration in Case 4, the ratio of $1.5 \cdot (T/K_I) = -0.2$ and $K_{II}/K_I \approx -0.01$, whereas for the final cracked configuration the ratio of $1.5 \cdot (T/K_I) = 0.5$ and $K_{II}/K_I \approx -0.01$. Following the red dotted lines in Figure 6, which correspond to these ratios, gives a better understanding of the magnitude of the crack turning when the crack is near or far from the doublers. The results of crack trajectory within the completely detailed model, using the ABAQUS interface, were compared with past analysis, which used the STAGS interface. This comparison showed that the resulting predicted crack trajectory was independent of the interface used.

This research has shown the ability to predict crack trajectory in a thin shell structure, but the inherent plane-stress or plane-strain assumption must be made. Also, a loss of fidelity in crack growth simulation occurs due to the homogenization of through-thickness crack shape. Therefore, this work will extend upon past thin-shell modeling of crack growth simulation by incorporating a fully 3D finite element model near the crack front. To maintain computational efficiency, regions of the model that are not near the crack front are modeled using shell elements. With this mixed-modeling technique, coupling of the shell region to the solid region is investigated. The mixed-modeling capability is facilitated by the discussed ABAQUS/FRANC3D interface and multi-point constraints defined within ABAQUS.

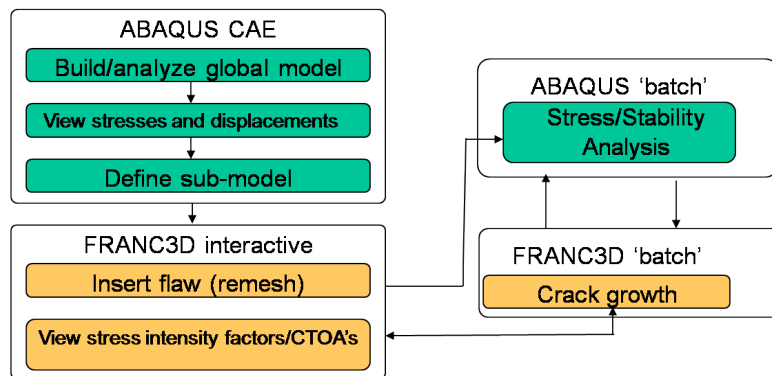


Figure 4: Iteration loop for crack growth modeling with the FRANC3D/STAGS framework [6].

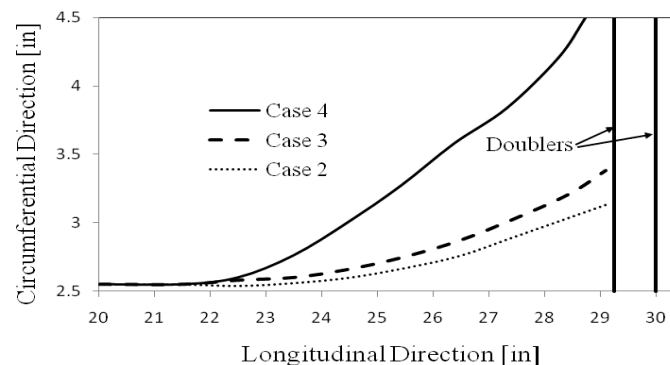


Figure 5: Predicted trajectory of crack in fuselage panel.

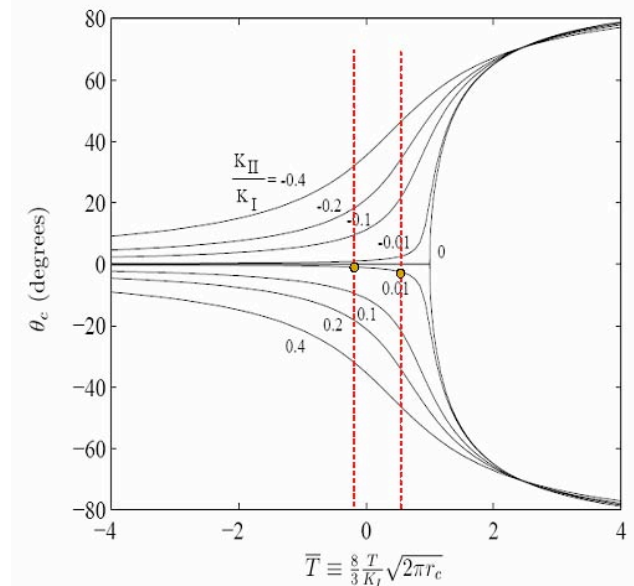


Figure 6: Influence of T-stress on propagation angle [6].

Acknowledgement

The authors would like to gratefully acknowledge the funding for this work provided by the NASA Integrated Resilient Aircraft Control project, NNX08AC50A.

References

- [1] Anderson TL. *Fracture Mechanics: Fundamentals and Applications*. CRC Press, Florida, 1994.
- [2] Brogan FA, Rankin CC, and Cabiness HD. Stags user manual. *Lockheed Palo Alto Research Laboratory, Report LMSC P, 32594*, 1994.
- [3] Chen CS, Wawrzynek PA, and Ingraffea AR. Residual strength analysis of fuselage structures subjected to widespread fatigue damage. *Proceedings of the Seventh International Fatigue Congress*, **4**, pages 2557–2562, 1999.
- [4] Chen CS, Wawrzynek PA, and Ingraffea AR. A methodology for fatigue crack growth and residual strength prediction with applications to aircraft fuselages. *Computational Mechanics*, **19**(6):527–532, 1997.
- [5] Chen CS, Wawrzynek PA, and Ingraffea AR. Prediction of residual strength and curvilinear crack growth in aircraft fuselages. *AIAA Journal*, **40**(8):1644–1652, Aug. 2002.
- [6] Chen CS. Crack Growth Simulation and Residual Strength Prediction in Thin Shell Structures. *Master's Thesis*. Cornell University, Ithaca, New York, 1999.
- [7] Chen CS, Wawrzynek PA, and Ingraffea AR. Residual strength prediction of aircraft fuselages using crack-tip opening angle criterion. *AIAA*, **40**(3):566–575, 2002.
- [8] Erdogan F and Sih GC. On the extension of plates under plane loading and transverse shear. *Journal of Basic Engineering*, **85**(4):519–527, 1963.
- [9] Kanninen MF and Popelar CH. *Advanced Fracture Mechanics*. Oxford University Press, New York, 1985.
- [10] Potyondy DO, Wawrzynek PA, and Ingraffea AR. Discrete crack growth analysis methodology for through cracks in pressurized fuselage structures. *International Journal for Numerical Methods in Engineering*, **38**(10):1611–1634, 30 May 1995.
- [11] Sih GC. *A special theory of crack propagation*, **XXI-XLV**. Noordhoff International Publishing, Netherlands, 1973.
- [12] Timoshenko SP and Woinowsky-Krieger S. *Theory of plates and shells*. McGraw-Hill Book Company, New York, 1959.
- [13] Viz MF, Potyondy DO, Zehnder AT, Rankin CC, and Riks E. Computation of membrane and bending stress intensity factors for thin, cracked plates. *International Journal of Fracture*, **72**(1):21–38, 1995.
- [14] Zehnder AT and Viz MJ. Fracture mechanics of thin plates and shells under combined membrane, bending, and twisting loads. *Applied Mechanics Reviews*, **58**(1):37–48, 2005.

Analysis of localized failure in metal beams and plates

Jaka DUJC, Boštjan BRANK*, Adnan IBRAHIMBEGOVIC

* University of Ljubljana, FGG
Jamova 2, 1000 Ljubljana, Slovenia
bbrank@ikpir.fgg.uni-lj.si

Abstract

We briefly present finite element framework for modeling of localized failures in ductile beams and plates. The embedded discontinuity finite element method is used. We model both diffused plasticity mechanism, which describes the first part of material nonlinear behavior, and the localized plasticity mechanism, that captures the softening phase of beam/plate response. Diffused plasticity is defined at the level of stress resultants with state variables describing general isotropic hardening. Local effects are captured in the form of softening plastic hinges or softening plastic lines. The plastic hinges and lines are defined as strong discontinuities of the generalized displacements at the element level and are treated as additional unknowns that can be eliminated element-wise from the global solution scheme. With a localized softening law we correlate strong discontinuities of the generalized displacements with stress resultants acting at the localization. Performance of presented formulations is illustrated with two numerical simulations.

1. Introduction

The ever increasing demand to build economically acceptable structures pushes design of structural systems to their limit. In this situation, the need to better understand the behavior of complex structural systems, including the failure modes, is enormous. This naturally leads to development of new models, which are capable of describing the localized effects, since the failure of a structure, or its components, usually occurs due to the localization of the yielding and damage.

2. Basics of beam/plate element with embedded discontinuity

We consider a displacement based finite element, with additional kinematic parameters $\boldsymbol{\alpha}$, which are introduced to describe discontinuity in displacements. Displacements over the element are then given as

$$\mathbf{u}(\mathbf{x}) = \sum_{i=1}^{nrnodes} \mathbf{N}_i(\mathbf{x}) \mathbf{u}_i + \mathbf{N}_\alpha(\mathbf{x}) \boldsymbol{\alpha}. \quad (1)$$

Interpolation functions are illustrated in Figure 1 for a 2-node bar element.

The strain field can then be computed as the space derivative of displacements

$$\boldsymbol{\varepsilon}(\mathbf{x}) = \sum_{i=1}^{nrnodes} \mathbf{B}_i(\mathbf{x}) \mathbf{u}_i + \mathbf{G}_\alpha(\mathbf{x}) \boldsymbol{\alpha} + \delta_{\mathbf{x}_{crack}} \boldsymbol{\alpha}, \quad (2)$$

where \mathbf{B}_i are strain displacement operators, and \mathbf{G}_α is strain operator related to $\boldsymbol{\alpha}$. If we drop the last term in (2) (one can interpret this term as localized plastic strain), we get the regular strains

$$\boldsymbol{\varepsilon}_R(\mathbf{x}) = \sum_{i=1}^{nrnodes} \mathbf{B}_i(\mathbf{x}) \mathbf{u}_i + \mathbf{G}_\alpha(\mathbf{x}) \boldsymbol{\alpha}. \quad (3)$$

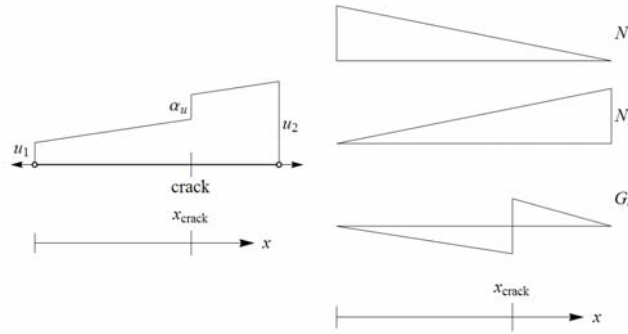


Figure 1: Two node bar element with embedded displacement discontinuity

To describe material behaviour, we consider three different material response regimes. The first one is purely elastic, the second one is classical plasticity or viscoplasticity and the last one covers the softening phase of structural response. By employing $\boldsymbol{\varepsilon}_R = \boldsymbol{\varepsilon}^e + \boldsymbol{\varepsilon}^p$, we can compute stress resultants $\boldsymbol{\sigma}$ at any point outside the discontinuity as

$$\boldsymbol{\sigma}(\mathbf{x}) = \mathbf{C}\boldsymbol{\varepsilon}^e(\mathbf{x}) = \mathbf{C}(\boldsymbol{\varepsilon}_R(\mathbf{x}) - \boldsymbol{\varepsilon}^p(\mathbf{x})), \quad (4)$$

where \mathbf{C} is elastic constitutive matrix, $\boldsymbol{\varepsilon}^e$ is elastic part of the corresponding deformation quantity, and $\boldsymbol{\varepsilon}^p$ are plastic strain-like variables. Activation and response of plastic regime is determined by the yield function (here q_h and ξ_h are variables controlling isotropic hardening)

$$\phi = \phi(\boldsymbol{\sigma}(\boldsymbol{\varepsilon}_R, \boldsymbol{\varepsilon}^p), q_h(\xi_h)) \leq 0, \quad (5)$$

evolution equations

$$\dot{\boldsymbol{\varepsilon}}^p = \dot{\gamma} \frac{\partial \phi}{\partial \boldsymbol{\sigma}}, \quad \dot{\xi}_h = \dot{\gamma} \frac{\partial \phi}{\partial q_h}, \quad (6)$$

and loading/unloading conditions. One can look at the softening phase as a special case of plasticity with one significant distinction, i.e. the plastic process is strictly limited to discontinuity. As in dispersed plasticity, we have yield function that governs the behavior of model in softening

$$\phi_\Gamma = \phi_\Gamma(\mathbf{t}(\boldsymbol{\alpha}), q_s(\xi_s)) \leq 0, \quad (7)$$

where \mathbf{t} is stress-resultant traction at discontinuity, while q_s and ξ_s are variables related to softening. Principle of maximum plastic dissipation gives the evolution equations

$$\dot{\boldsymbol{\alpha}} = \dot{\gamma}_\Gamma \frac{\partial \phi_\Gamma}{\partial \mathbf{t}}, \quad \dot{\xi}_s = \dot{\gamma}_\Gamma \frac{\partial \phi_\Gamma}{\partial q_s}, \quad (8)$$

where γ_Γ is plastic multiplier for localized plasticity.

By using the weak form of equilibrium equations, one can obtain a set of global equations

$$A_{e=1}^{n_{elements}} [\mathbf{f}^{int,e} - \mathbf{f}^{ext,e}] = \mathbf{0}, \quad \mathbf{f}^{int,e} = \int_{\Omega^e} \mathbf{B}_i^T \boldsymbol{\sigma} d\Omega^e. \quad (9)$$

Along with the usual form of global equilibrium equations (9), we get additional element-wise equilibrium equations, which state, that the stress-resultant traction in the discontinuity must be in equilibrium with surrounding stress resultant field

$$\forall e: \quad \mathbf{h}^e = \int_{\Omega^e} \mathbf{G}_\alpha^T \boldsymbol{\sigma} d\Omega + \int_{\Gamma^e} \mathbf{t} d\Gamma^e = \mathbf{0}, \quad (10)$$

where Γ^e is the discontinuity. Eqs. (9) and (10) are solved as described in Ibrahimbegovic [4] and Ibrahimbegovic and Melnyk [1].

2. Numerical examples

As a first example we consider plate with length $L=10$, width $b=5$ and thickness $h=1$. Plate is clamped along one of the shorter edges. Transversal displacement is incrementally applied at the opposite end. Plate's response is initially linear elastic with Young's modulus $E=1$ and Poisson's ratio $\nu=0.3$, until the yield function is violated and the softening line forms. The response of the hinge line is determined with yield function

$$\phi_\Gamma = |m_{crack}| - (m_u - q_s) \leq 0, \quad (11)$$

where $m_{crack} = \mathbf{t} \cdot \mathbf{n}$, \mathbf{t} is stress-resultant (moment) traction at discontinuity, \mathbf{n} is the unit normal vector (it is determined with the direction of principal bending moment) to the hinge line Γ and $m_u = 0.00025$ is the ultimate bending strength. We assume linear softening law with softening modulus $K_s = 0.008$. In Figure 2 we plot the reaction-displacement curves for several meshes. Figure 3 presents hinge line patterns for different meshes.

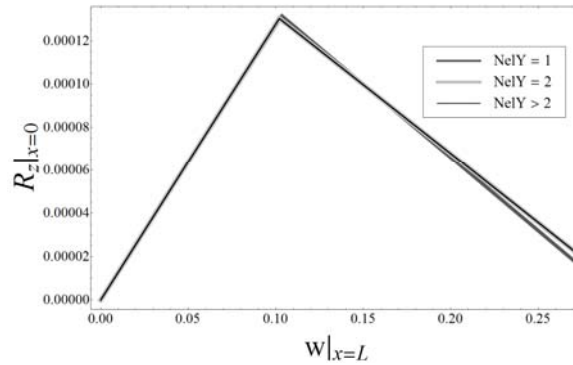


Figure 2: Rectangular plate - reaction-displacement curves

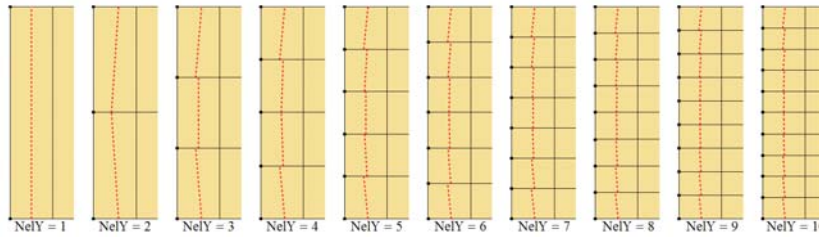


Figure 3: Hinge lines for different meshes (only the area near support is plotted)

In the second example we consider a beam with the following geometric and material properties: length $L=10$, $EI=1$, yield moment $M_y=0.004$, hardening modulus $K_h=0.05$, ultimate moment

$M_u = 0.005$, and softening modulus $K_s = 0.04$. The beam is clamped at one end; transversal displacement is incrementally applied at the opposite end. The plastic response is determined with yield function

$$\phi = M / -(M_y - q_h) \leq 0, \quad (11)$$

and the plastic hinge response is determined with

$$\phi_{\Gamma} = M_{crack} / -(M_u - q_s) \leq 0, \quad (11)$$

where $M_{crack} = M|_{x=x_{crack}}$. We assume linear hardening and linear softening. Figure 3 presents reaction moment-displacement curve obtained with 4 Euler – Bernoulli beam elements.

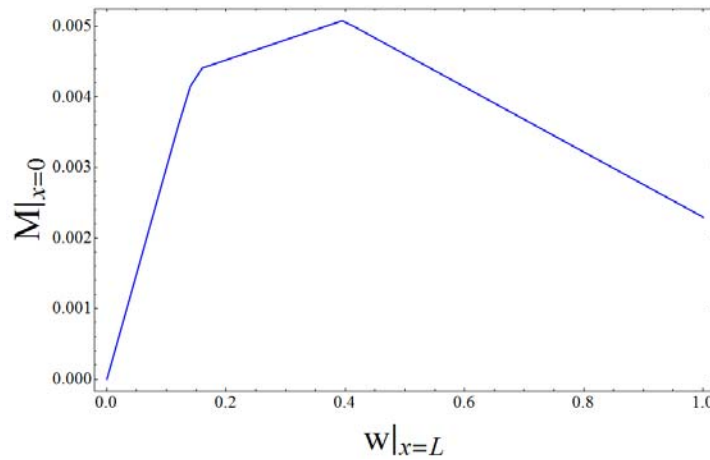


Figure 3: Built-in beam - reaction moment-displacement curve

3. Conclusions

We have presented basics of finite element formulation with embedded discontinuities for metal beams and plates. The formulations are similar to those presented in Ehrlich and Armero [2], [5] and Armero and Ehrlich [3]. Further details of our work and further numerical examples will be presented at the conference.

References

- [1] Ibrahimbegovic A., Melnyk S., 'Embedded discontinuity finite element method for modelling of localized failure in heterogeneous materials with structured mesh: an alternative to extended finite element method', *Comput Mech*, 40, 149-155, (2007).
- [2] Ehrlich D., Armero F., 'Finite element methods for the analysis of softening plastic hinges in beams and frames', *Comput Mech*, 35, 237-264, (2005).
- [3] Armero F., Ehrlich D., 'Numerical modeling of softening hinges in thin Euler-Bernoulli beams', *Computers and Structures*, 84, 641-656, (2006).
- [4] Ibrahimbegovic A., 'Mécanique non linéaire des solides déformables: formulation théorique et implémentation éléments finis', *Hermes Science-Lavoisier*, (2006).
- [5] Armero F., Ehrlich D., 'Finite element methods for the multi-scale modeling of softening hinge lines in plates at failure', *Comput. Methods Appl. Mech. Engrg.*, 195, 1283-1324, (2006).